Universität Bremen

Master Thesis

Measurement of NO_2-profiles using a drone-mounted DOAS-spectrometer

submitted by:

Nina Lühning

6055390

First assessor: **Dr. Andreas Richter**

Second assessor: **Prof. Dr. Mihalis Vrekoussis**

Institute of Environmental Physics

University of Bremen

Bremen, 16th September 2026

Contents

1 Introduction **3**

2 Theoretical Background **5**
2.1 Dynamics of quadcopters 5
2.2 NO_X in the atmosphere 7
2.3 DOAS 8
2.3.1 Optics 8
2.3.2 Principle 12
2.3.3 Geometry 14

3 Hardware **16**
3.1 Pre-existing structure 16
3.2 DOAS setup 18
3.2.1 The Spectrometer 18
3.2.2 The optical fibre 20
3.3 Total payload and flight time 23

4 Software **24**

5 Calibration measurements **27**
5.1 Characterization of the spectrometer 27
5.1.1 Dark measurements 27
5.2 Linearity of the detector 28
5.2.1 Calibration using a HgCd lamp 30
5.2.2 Temperature dependency 32
5.2.3 Straylight 34
5.2.4 Polarization 36
5.3 Calibration of the telescope lens 38
5.4 Angle calibration 40

6 Test measurements **44**
6.1 Tests with an NO_2 cell 44
6.2 Long-term measurement 46

7 Field measurements **48**
7.1 Results of the flight on the 13^{th} of July 2026 49

7.2 Results of the flight on the 3rd of August 2026 54

8 Improvements and outlook **57**

9 Conclusion **60**

References **64**

Appendix I: Groundstation plots **65**

13.07.2026 65

03.08.2026 66

Appendix II: Instructions **66**

Assembly guide 66

Quick guide to the Raspberry Pi 75

1 Introduction

Nitrogen oxides and other trace gases emitted by industry, traffic and other sources are, either as direct or indirect greenhouse gases, responsible for the anthropogenic climate change. Due to their impact on the environment and also human health, it is important to know the concentration and distribution of the emitted trace gases. Therefore, it is useful to measure the spatial distribution of emission plumes.
One method to measure the trace gas concentration in the atmosphere is differential optical absorption spectroscopy (DOAS), a spectroscopy method that isolates the narrowband absorption structures of trace gases from broadband effects in the atmosphere and compares the absorption at different wavelengths. DOAS measurements can be and are performed using different measuring platforms and setups. While the vertical distribution of trace gases have been measured using ground-base multi-axis DOAS (Friedrich et al. 2019) or satellite measurements (Horner et al. 2024), measurements using unmanned aerial vehicles (UAVs) have gained popularity in recent years.
Nowadays, drones and other unmanned vehicles are common platforms for emission measurements in urban and rural areas, especially ones that cannot be accessed safely like volcanoes. Although their usage is regulated and limited, their agility and freedom of movement allows them to easily measure the spatial distribution of trace gases, which makes them a viable option.
One common approach is to use an in-situ sensor and to fly directly through the plume. This has been done amongst other to measure CO_2 (Reuter et al. 2021), SO_2 (Rüdiger et al. 2018), O_3 (Lee, Hwang, and Lee 2022) and NO_2 (Fernando and Adams 2025). However, there have also been measurements from far away using a spectrometer and the DOAS method (e. g. Stix et al. 2018, Liu et al. 2019 or Womack et al. 2022). Unmanned aerial vehicles represent, therefore, a possibility to determine a vertical profile of trace gases using the DOAS method.

In this thesis, a measurement system using an unmanned aerial vehicle was developed to complement ground-based and aircraft-based DOAS measurements. The new Drone-DOAS-system is mounted a DJI Matrice 210v2 previously used in measurements done by Reuter et al. (2021) and is a modification of their measurement system, referred to as the CRUSOE-system. The structure is created to be modular so that both setups can be used. For the system, a new compact Avantes Nexos Spectrometer was purchased and used to replace the CO_2 sensor of the CRUSOE-system. Further hardware needed for

the DOAS measurements was designed as well. The measurements run on the Raspberry Pi 3B+, which is also used by the CRUSOE-system with an updated operating system. The software of the CRUSOE-system are Python scripts. For the Drone-DOAS-system, these scripts are updated and supplemented by new ones for the measurements with the spectrometer. The hardware and software of the system was characterized, calibrated and tested in flight-like conditions.
Lastly, the new drone-DOAS measurement system was used to conduct two flights in the Niedervieland area in Bremen-Seehausen to measure the NO_2 profile of the plume emitted by the steel works.

2 Theoretical Background

2.1 Dynamics of quadcopters

A quadcopter is an unmanned aerial vehicle (UAV) with four propellers, each controlled independently by a DC motor. When the propeller rotates, it creates a torque Q around it own axis, causing the vehicle to counter-act this rotation by rotating in the opposite direction. To prevent this, two of the propellers rotate clockwise, while the other two rotate counter-clockwise, as shown in Fig. 2.1.

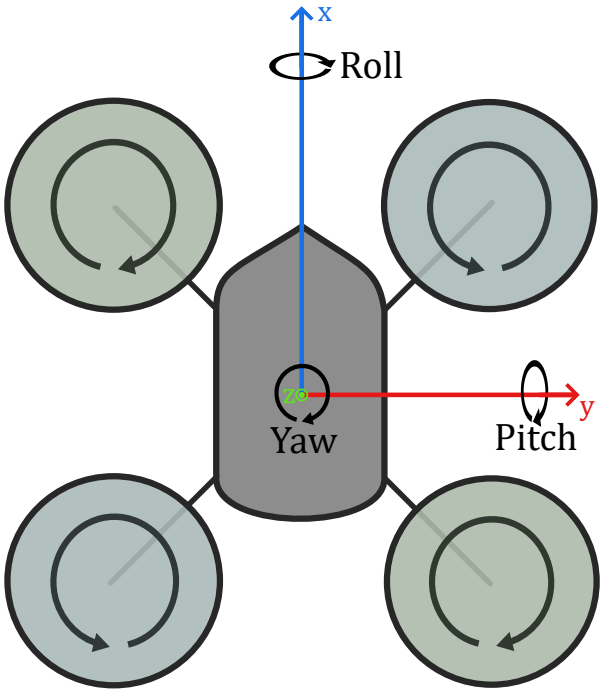


Figure 2.1: A sketch of an UAV showing the spin direction of the propellers and the orientation of the roll, pitch and yaw.

Thus, the total angular momentum of the vehicle is near zero while hovering.
Each rotor produces a thrust T_i through the torque Q_i applied by a motor. This torque Q_i can be described as

$$Q_i = K_q I_i \tag{2.1.1}$$

with I_i being the current running through the i-th motor and K_q a motor specific con-

stant. Thus, with the voltage U_i across the motor, it produces the power P_i

$$P_i = I_i U_i = \frac{Q_i}{K_q} U_i \tag{2.1.2}$$

In a stationary state, the power P_i has to be equal to the ideal power $P_{\text{hover, i}}$ required to generate thrust by increasing the momentum of the column of air underneath the propeller. At hover this is

$$P_{\text{hover, i}} = T_i v_{\text{hover, i}} \tag{2.1.3}$$

$v_{\text{hover, i}}$ is the induced velocity, that describes the change in air speed induced by the rotor. In general, $v_{\text{hover, i}}$ can be described as

$$v_{\text{hover, i}} = \sqrt{\frac{T_i}{2\rho_{\text{air}} A}} \tag{2.1.4}$$

with ρ_{air} being the density of air and A the area swept by the rotor.
The torque Q_i is proportional to the thrust T_i with a constant κ that depends on the blades geometry. Together with (2.1.2), (2.1.3) and (2.1.4), this gives

$$\frac{\kappa T_i}{K_q} U_i = K T_i U_i = T_i \sqrt{\frac{T_i}{2\rho_{\text{air}} A}} \tag{2.1.5a}$$

with the two constants κ and K_q summarized in K, which can be rearranged to

$$T_i = 2K^2 U_i^2 \rho_{\text{air}} A \tag{2.1.5b}$$

Therefore, each propeller produces a thrust T_i controlled by the applied voltage U_i. The total thrust T of all four propellers has to equal the gravitational force $F_{\text{g,UAV}}$ of the UAV for it to hover. If T exceeds $F_{\text{g,UAV}}$ by increasing the total voltage U, the UAV rises, and it descends if T is smaller than $F_{\text{g,UAV}}$ (Hoffmann et al. 2007).
The flight time of the UAV is limited by the available power of the batteries. Furthermore, the flight time is affected by the mass of the vehicle, since more thrust is required for heavier UAVs, causing a higher power consumption. Also strong winds can reduce the total flight time as the UAV has to work against them to keep itself stable, draining the batteries even more (Mueller 2025). Figure 2.1 shows the three possible kinds of rotations the vehicle can perform around one of its axes. These rotations are realized

by a difference in thrust created by slowing down or speeding up individual propellers, as shown in Fig. 2.2 (Abougarair, Almgallesh, and Shashoa 2024). Increasing the ro-

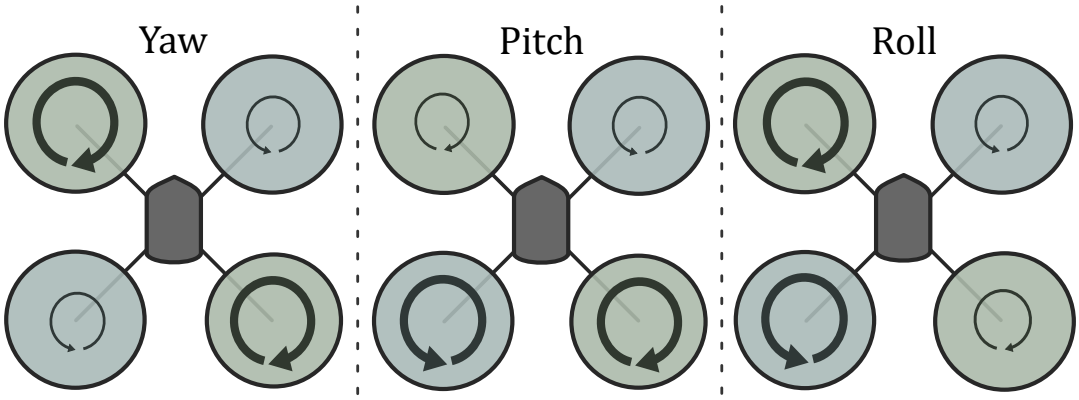


Figure 2.2: The change in rotor rotation to perform the yaw, pitch and roll rotations.

tation frequency of the two back propellers, while decreasing the rotation frequency of the front propellers, causes the UAV to lean and move forward, which is called pitch motion. A roll motion is performed by increasing or decreasing the rotation frequency of the propellers on one side of the UAV causing it to move sideways. Lastly, to rotate the UAV along its vertical axis, the rotation frequency of two propellers diagonally from each other are increased (Kartal 2026).

2.2 NO_X in the atmosphere

The most relevant nitrogen oxides NO_X are NO and NO_2. At high temperatures, nitrogen N_2 and oxygen O_2 in the atmosphere can combine to NO_X. This can happen naturally, e.g. by lightning, but a more prominent source in the troposphere is as a by-product of combustion processes of traffic and industry. NO_X have an impact on the environment in two ways. On one hand, they can cause acid rain, depositing the acid into various ecosystems. This results e.g. in the acidification of water bodies. On the other hand, when NO_X is exposed to solar ultra-violet (UV) radiation, high concentrations tropospheric ozone O_3 are formed, which makes it an indirect green house gas (Tian 2025).

During daytime, exposure to UV radiation with the energy $h\nu$ causes the photolysis of

NO_2 to NO and O. The formed O radical then reacts with O_2 to form O_3

$$NO_2 + h\nu \rightarrow NO + O \tag{2.2.1a}$$

$$O + O_2 \rightarrow O_3 \tag{2.2.1b}$$

Thus, for each photolysed NO_2 molecule one O_3 molecule is formed. The created NO is oxidized by O_3 to NO_2

$$NO + O_3 \rightarrow NO_2 + O_2 \tag{2.2.2}$$

This creates an equilibrium between NO_2, NO and O_3, with no net formation of ozone. The concentrations of these three molecules can be described by the relation

$$\frac{[NO]}{[NO_2]} = \frac{j}{k[O_3]} \tag{2.2.3}$$

with j being the photolysis rate of NO_2 and k the rate constant for the reaction of ozone with NO. In the polluted troposphere, NO can also be converted back to NO_2 by reacting with other free radicals and not with the formed O_3. The NO_2 gets photolysed again, resulting in a net ozone production. In the stratosphere on the other hand, the main source of NO_X is the oxidation of biogenic N_2O. Here, the NO_X cycle has the opposite effect and causes a reduction of stratospheric ozone in the ozone layer.
NO_2 has a short atmospheric life time of a few hours to days. Consequently, the distribution of NO_2 in the atmosphere is determined by degradation and atmospheric transport processes. Depending on the wind conditions, this can lead to high NO_2 concentrations close to the emission source, which decrease sharply with the distance. NO_2 is often emitted alongside CO_2. The longer atmospheric life time of CO_2, ranging from years to decades, results in a more even distribution. Therefore, NO_2 can be used as a tracer to locate CO_2 emission sources (Roedel 2024).

2.3 DOAS

2.3.1 Optics

Applications of differential optical absorption spectroscopy (DOAS) use grating spectrometers to measure the spectra of natural or artificial light sources. To ensure a more consistent light coupling, an optical fibre is placed in front of the spectrometer's slit. Additionally, the field of view can be limited by using a telescope lens.

Grating spectrometers use reflection or transmission gratings to split a light source into its individual spectral components. These kinds of spectrometer can have a compact design while still having a high enough spectral resolution.
When light hits an obstacle, it gets diffracted, due to the wave nature of light. According to the Huygens' principle, every point of the wavefront is the source of a spherical wave. Thus, a plane wave hitting a single slit propagates in all directions behind the the slit. Interference between the spherical waves result in a diffraction pattern alternating between minima and maxima. For maxima to occur, the path length difference of two waves has to be an integer multiple of the wavelength λ.
If the number of slits is increased, the number of maxima of the diffraction pattern increases as well. For a grating with the grating constant g, shown in Fig. 2.3, the m-th maxima are described by

$$\sin(\phi_m) = \frac{m\lambda}{g} \tag{2.3.1}$$

Therefore, the diffraction angle ϕ_m depends on the wavelength λ with longer wavelengths being diffracted stronger. For the zeroth order, the maxima for all λ coincide. For higher diffraction orders, the spreading of the spectrum becomes larger, as well as less intense. In a spectrometer, usually only one diffraction order is used.

The detector of the spectrometer measures a relative spectrum of the light source in

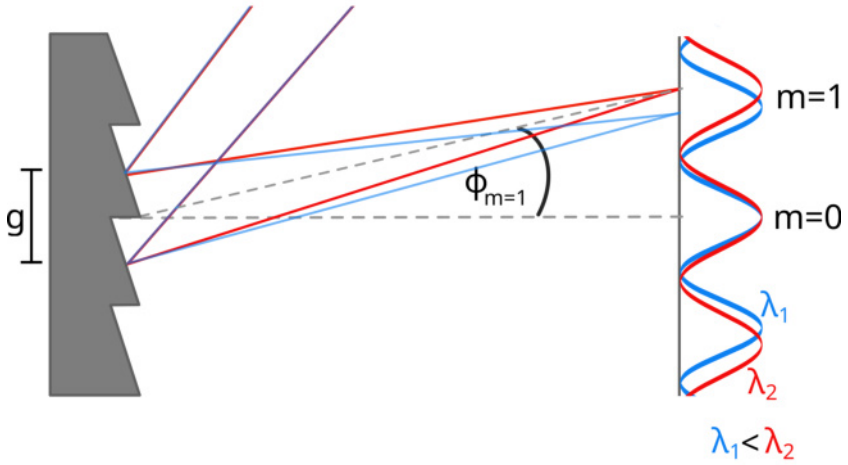


Figure 2.3: A sketch showing the diffraction of two different wavelengths at a grating with a grating constant g for the 0^{th} and 1^{st} order.

pixels. To get the absolute spectrum, a spectral lamp with a known spectrum is used to

get the relation between the pixels of the detector and the wavelength (Vollmer 2025). Light entering the spectrometer can come from any direction, creating an inconsistency in intensity and in general an imprecise coupling of light. To combat this and to be more flexible, an optical fibre is placed in front of the opening of the spectrometer. Optical fibres use the principle of total internal reflection to transmit a light beam from one end of the fibre to the other. A simple step index fibre, shown in Fig. 2.4, consists of a core and surrounding cladding with the refractive indices n_1 and n_2 respectively, where $n_1 > n_2$ (Meschede 2008).

A beam of light entering the core of the fibre at an angle α, that is smaller than the

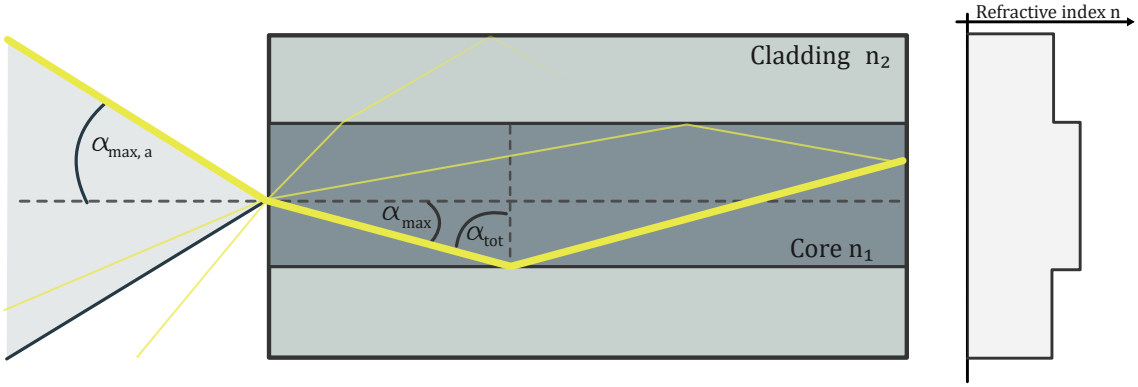


Figure 2.4: The cross-section of a step index fibre with the maximum angle of acceptance $\alpha_{\text{max,a}}$ outside the fibre, the maximum angle α_{max} inside the fibre and the critical angle α_{tot} of the total internal reflection.

critical angle α_{tot}, gets fully reflected when hitting the boundary of the optically denser medium, confining it to the core. A beam with an angle α greater than α_{tot} gets partially transmitted to the cladding and does not propagate to the other end. The angle α_{tot} of total reflection is defined as

$$\alpha_{tot} = \arcsin\left(\frac{n_2}{n_1}\right) \tag{2.3.2}$$

and is the angle at which the refracted light beam has an angle of 90 °.
Light entering the fibre at the maximum angle of acceptance $\alpha_{\text{max,a}}$ gets refracted according to the law of refraction

$$n_0 \sin(\alpha_{\text{max,a}}) = n_1 \sin(\alpha_{\text{max}}) = n_1 \cos(\alpha_{\text{tot}}) \tag{2.3.3}$$

with $\alpha_{\max} = \alpha_{\text{tot}} - 90\,^\circ$ as the maximum acceptance angle inside of the fibre and n_0 the refractive index of air. Using the trigonometric relation $\cos(\alpha) = \sqrt{1 - \sin(\alpha)^2}$ and Eq. (2.3.2), the right side can be written as

$$n_0 \sin(\alpha_{max,a}) = n_1 \sqrt{1 - \sin(\alpha_{tot})^2} = n_1 \sqrt{1 - \left(\frac{n_2}{n_1}\right)^2} \tag{2.3.4a}$$

$$n_0 \sin(\alpha_{\text{max,a}}) = \sqrt{n_1^2 - n_2^2} = NA \tag{2.3.4b}$$

This results in a relation between the maximum angle of acceptance $\alpha_{\text{max,a}}$ and the refractive indices of core and cladding of the optical fibre that is referred to as the numerical aperture NA. The numerical aperture characterizes the opening of an optical system and determines the acceptance angle of light, that is guided in the fibre, as well as the divergence of the beam when exiting the fibre (Demtröder 2013). In a step index fibre with a circular cross-section, two perpendicular linearly polarised waves propagate at the same speed. However, tension in the fibre, causes birefringence in the material. As a consequence, the propagation speed of the two polarisation states differ. This changes the polarisation state of a linearly polarised wave unpredictably while propagating through the fibre. Special fibres can maintain the polarisation of the wave by deliberately distorting the refractive index of the fibre core in an elliptic shape. The efficiency of the spectrometer is dependent on the polarization state of the incoming light, requiring the polarization of the light to be as low as possible.
Using an optical fibre to couple light into the spectrometer has the additional advantage that a lens can be added to it. If a light source is far away, the beams can be assumed to be parallel. A lens with the focal length f units the parallel light beams of the light source in its focal point. This can be used to have a more focussed light beam coupled into the fibre (Meschede 2008).

Light focussed by a thin lens can be described as a Gaussian beam, since its transversal intensity profile resembles a Gauss curve. Shown in Fig. 2.5, the radius ω of a beam of light is generally not constant, but has a minimum, the waist ω_0, close to the lens and gradually increases afterward. Along the optical axis z with the beam waist ω_0 at $z = 0$, the beam radius ω changes according to

$$\omega^2(z) = \omega_0^2 \left(1 + \left(\frac{z}{z_0}\right)^2\right) \tag{2.3.5}$$

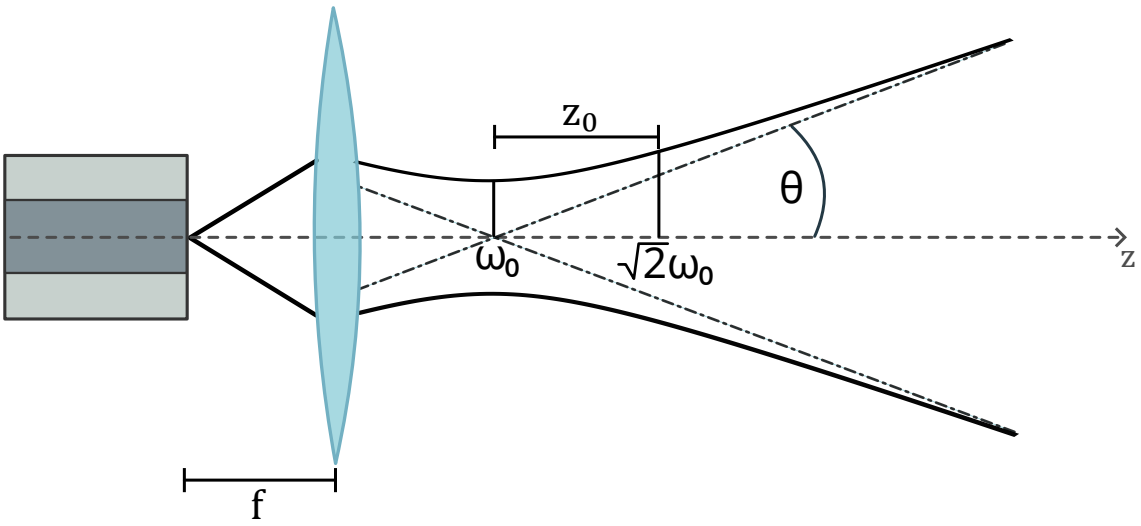


Figure 2.5: The Gaussian beam focused by a lens with a focal length f. The beam has a waist ω_0 and a Rayleigh length z_0. It diverges with the angle θ.

with Rayleigh distance z_0. The Rayleigh distance z_0 describes the near field of the smallest beam cross-section and is the length at which the cross-section of the beam has doubled with respect to the square of the beam waist ω_0^2, resulting in $\omega(z_0) = \sqrt{2}\omega_0$. For light with the wavelength λ, the Rayleigh distance z_0 is

$$z_0 = \frac{\pi\omega_0^2}{\lambda} \tag{2.3.6}$$

In the far field for $z >> z_0$, (2.3.5) can be approximated by the linear $\omega(z) = \frac{\omega_0 z}{z_0}$. Using this approximation, the beam diverges with an angle θ from the optical axis

$$\tan(\theta) = \frac{\omega_0}{z_0} \tag{2.3.7}$$

In practice, light is coupled into the lens, which does not correspond to a Gaussian beam. However, using the divergence angle θ and Eq. (2.3.4b), conclusions can be made about the optical system (Löffler-Mang 2012).

2.3.2 Principle

While propagating through an absorber filled volume with a path length L, light with an initial intensity $I_0(\lambda)$ gets absorbed according to the Lambert-Beer's law

$$I(\lambda) = I_0(\lambda)\exp\left[-L\sigma(\lambda)c\right] \tag{2.3.8}$$

with σ being the wavelength-dependent absorption cross-section, that is characteristic for each trace gas. Using the Lambert-Beer's law, the concentration c of the absorber in the volume can be calculated

$$c = \frac{\ln\left(\frac{I_0(\lambda)}{I(\lambda)}\right)}{\sigma(\lambda)L} = \frac{D}{\sigma(\lambda)L} \tag{2.3.9}$$

The natural logarithm of the two intensities $I(\lambda)$ and $I_0(\lambda)$ can be summarized as the optical density D, which characterizes the extinction of light. In order to obtain both intensities $I(\lambda)$ and $I_0(\lambda)$, measurements have to be taken with and without the absorber respectively. This is impossible in the atmosphere. Differential optical absorption spectroscopy (DOAS) overcomes this problem by comparing the differences in absorption at different wavelengths λ.

In the atmosphere, light experiences extinction by means other than just absorption by a single trace gas i. Due to the presence of various other gases and aerosols, a beam of light can be either Mie or Rayleigh scattered, described by the scattering cross-sections $\sigma_M(\lambda)$ and $\sigma_R(\lambda)$ respectively and widened due to turbulences. The turbulences, as well as effects caused by the measuring device, are collected in a quantity $A(\lambda)$. Thus, (2.3.8) is expanded to

$$I(\lambda) = I_0(\lambda)\exp\left[-L\sum_i (sigma_i(\lambda)c_i + \sigma_M(\lambda) + \sigma_R(\lambda)\right] A(\lambda) \tag{2.3.10}$$

Effects, like scattering and turbulences, have broadband characteristics, that vary only slowly with the wavelength λ, while the absorption of trace gases have narrow structures. This can be used to split Eq. (2.3.10) by separating the absorption cross-section $\sigma_i(\lambda)$ into the slowly varying broadband characteristics σ_{i_0} and the narrowband trace gas absorption $\sigma_i'(\lambda)$, resulting in

$$I(\lambda) = I_0(\lambda)\exp\left[-L\sum_i \sigma_i'(\lambda)c_i\right]\exp\left[-L\sum_i \sigma_{i_0}(\lambda)c_i + \sigma_M(\lambda) + \sigma_R(\lambda)\right] A(\lambda)$$

$$I(\lambda) = I_0(\lambda)\exp\left[-L\sum_i \sigma_i'(\lambda)c_i\right] A'(\lambda) \tag{2.3.11a}$$

with the scattering and turbulences summarized in $A'(\lambda)$. Substituting the optical density D and cross-section $\sigma(\lambda)$ by the differential quantities D' and $\sigma_i'(\lambda)$, a differential optical density D' can be obtained in analogy to Eq. (2.3.9)

$$D' = \ln\left(\frac{I_0(\lambda)}{I(\lambda)}\right) = L\sum_i \sigma_i'(\lambda)c_i + \sum_j c_j\lambda^j \tag{2.3.12a}$$

$$= \sum_i \sigma_i'(\lambda)SC_i + \sum_j c_j\lambda^j \tag{2.3.12b}$$

with the path length L and the concentration of a trace gas c_i combined to the differential slant column density SC_i. The differential slant column density SC_i can then be retrieved by fitting to the optical density D' (Platt 2026).

2.3.3 Geometry

DOAS measurements can be performed using many different viewing geometries. A common method for ground-based measurements is Multi-Axis DOAS (MAX-DOAS). MAX-DOAS takes a series of off-axis measurements at different elevation angles α. This results in a change of the observed slant column of a trace gas as a function of α, providing information about the vertical distribution of the trace gas.
This method can also be used for aircraft-based measurements, extending the elevation angles α downwards. Other commonly used viewing geometries for measurements with aeroplanes are the nadir and limb geometries. Measurements utilizing the nadir geometry capture a large area below the aircraft using back-scattered light from the surface. For limb measurements, the telescope is pointed perpendicular to the flight direction, taking advantage of long light paths. In general, aircraft-based measurements have the advantage, that the vertical distribution of trace gases can be measured during ascend and descend of the aeroplane. However, the exact roll and pitch angles α_{roll} and α_{pitch} of the aircraft have always to be known (see e.g. Schönhardt et al. (2015) or Prados-Roman et al. (2011)).

The aircraft-based measurements in this thesis use an unmanned aircraft. The most common approach is to utilize the ascend and descend of the UAV to measure a vertical distribution of a trace gas using a sensor (e. g. Reuter et al. 2021 or Fernando and Adams 2025). Another approach is using miniature spectrometers and performing DOAS measurements. This has been done to measure the SO_2 flux of volcanoes by

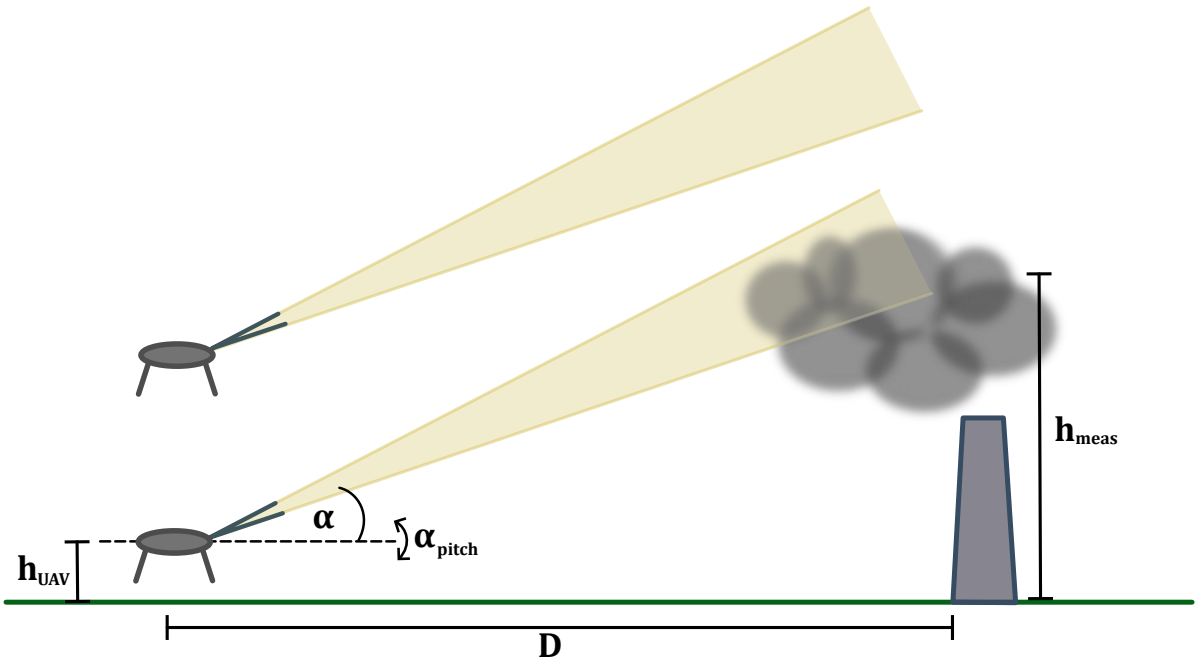


Figure 2.6: The vertical geometry of a measurement, with an UAV at a height h_{UAV} and distance D to a source. The measured height h_{meas} is further dependent on the pitch angle α_{pitch} and the angle α of the optical fibre.

Rüdiger et al. (2018) and Stix et al. (2018). The measurements were performed facing vertically upwards and transecting the plume at a distance to the source. Both of these approaches traverse the plume directly.
In this thesis, the drone-DOAS measurements use a viewing angle α, that can be adjusted between 0°, looking horizontally, and 90°, looking vertically upwards. The UAV does not traverse the plume, instead the lateral profile of the plume is measured at a distance D, as shown in Fig. 2.6. The spatial distribution of the plume is measured by vertical and horizontal movement of the UAV. Like the measurements with an aeroplane, the roll and pitch angles α_{roll} and α_{pitch} are important to known. Since the maximum flight height $h_{\mathrm{UAV,max}}$ of the UAV is limited, the angle α of the telescope can be adjusted to gain more height. At a distance D to the plume, the measured height h_{meas} is

$$h_{\mathrm{meas}} = D \tan\left(\alpha + \alpha_{\mathrm{pitch}}\right) + h_{\mathrm{UAV}} \tag{2.3.13}$$

when the telescope is looking to the front of the UAV. If the telescope looks to the side of the UAV, α_{roll} has to be added instead.

3 Hardware

3.1 Pre-existing structure

The CRUSOE-system is an unmanned aircraft system to derive CO_2 emissions of anthropogenic point sources (Reuter et al. 2021). The Drone-DOAS-system developed in this thesis is a modification of the CRUSOE-system, building upon its pre-existing structure. The modifications are kept modular and none of the Drone-DOAS attachments are permanent. Therefore, the setup to measure CO_2 emissions can still be used and, if desired, either measurement can be conducted.

The drone used is a DJI Matrice 210v2. The UAV is powered by two lithium polymer batteries, each with a capacity of 7660 mAh, shown in Fig. 3.1. With the batteries, the UAV has a mass of about 4.8 kg and a maximum flight time of 34 min, which is reduced to 24 min by adding 1.34 kg of additional payload. In order to attach the payload, the UAV has four mounting threads on its top cover and two bayonet-mounts on its underside.

The manufacturer specifies that the UAV can operate in temperatures between -20 °C and 50 °C and has a maximum wind resistance of 12 $\frac{m}{s}$. With special propellers, the UAV could potentially reach a maximum flight altitude of 3 km, but it is limited by its firmware to 500 m above ground level and to 120 m by legal restrictions.



Figure 3.1: Picture of the UAV without attachments. The UAV has a height of 30 cm and a length of 60 cm with the arms extended.

An aluminium measurement platform can be mounted on the drone, that contains a small computer, sensors and part of Drone-DOAS-system, shown in Fig. 3.2. Most of the sensors of the CRUSOE-System are permanently mounted to the measurement platform and therefore, are used for the Drone-DOAS-system as well.
These sensor include an FT205 anemometer by FT Technologies. This is a 2D ultrasonic acoustic resonance anemometer, which is used to measure the wind speed specifically on drones and has a specified accuracy of $\pm 0.3\,\frac{\mathrm{m}}{\mathrm{s}}$. To minimise the effects of the movement of the rotor, the anemometer is mounted on top of a 36 cm high carbon fibre pole in the middle of the measurement platform.
Additionally, there are two Adafruit sensors on the measurement platform, the Bosch BMP388 and the Sensirion SHT31-DIS. These two sensors measure the pressure, the temperature and the relative humidity during the flight with an accuracy of $\pm 0.5\,\mathrm{hPa}$, $\pm 0.3\,^{\circ}\mathrm{C}$ and $\pm 2\,\%$ respectively.
The status of the measurements is indicated by three LEDs (red, yellow and green), which are located on the measurement platform.

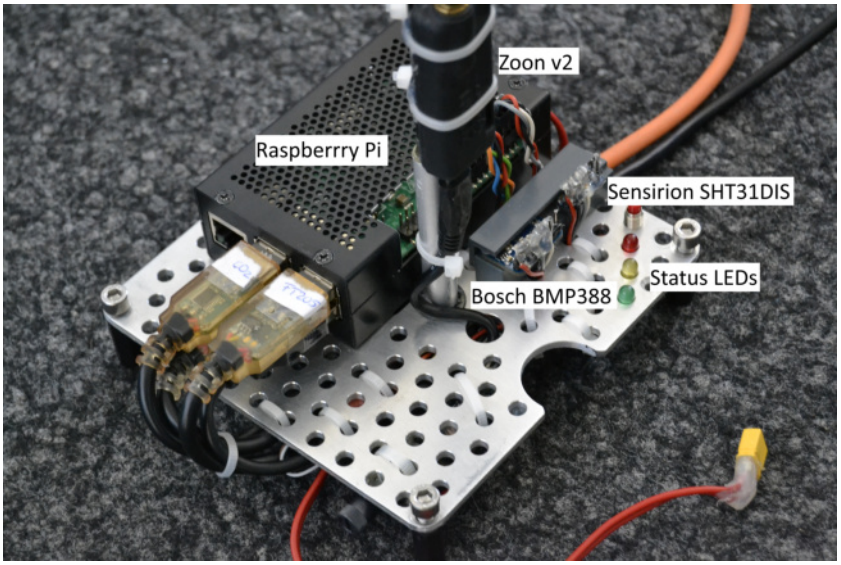


Figure 3.2: Picture of the measurement platform without the drone-DOAS additions.

All measurements are controlled by a Raspberry Pi 3B+, a single chip computer which is connected to the instruments and the drone itself. The Raspberry Pi is powered by the batteries of the UAV. The power provided by the batteries can be inconsistent and disturb the measurements by causing a power failure of the Raspberry Pi. To prevent this, an expansion board for the Raspberry Pi, a JOY-IT Strompi 3, is used. The expansion

board regulates the power provided by an inconsistent source and ensures a constant power supply. In addition to the power supply, the Raspberry Pi is also connected to the UAV via a UART to USB-converter. This connection allows the Raspberry Pi to access the GPS data of the UAV, as well as information about the orientation and velocity of the drone during the flight.

In addition to the sensors, the measurement platform includes a Dronee Zoon v2 telemetry module, which is connected to the Raspberry Pi as well. This is a small antenna, which enables communication between the Raspberry Pi and a computer on the ground. It has a transmission range of up to 3 km and, due to its small bandwidth, can only transmit a limited amount of data. This makes it possible to review the data during the flight, allowing to see whether the plume is in the field of view of the telescope and to adjust the flight accordingly. It also serves as a safeguard to keep some data, if either the Raspberry Pi or the UAV crash.

3.2 DOAS setup

The CRUSOE-System is designed to measure CO_2 using an in-situ sensor mounted to the underside of the UAV. For the Drone-DOAS-system, the sensor is replaced by a compact spectrometer used to measure NO_2 remotely. Fig. 3.3 shows the general setup of the Drone-DOAS-system. It consists of the spectrometer on the underside of the UAV, that is connected to the Raspberry Pi on top of it. To collect the light, an optical fibre is on one end mounted to the spectrometer and at the other end, to the measurement platform also on top of the UAV.

3.2.1 The Spectrometer

For the DOAS measurements an Avantes Nexos Spectrometer is used. This is a compact spectrometer with a length of 10.5 cm, a width of 8 cm and a height of 2 cm. It has a mass of 265(1) g and is therefore well suited for measurements with an UAV. The spectrometer uses a 2048 pixel CMOS detector and has a wavelength range from 300 nm to 455 nm, specified by the manufacturer. Although the ideal range for NO_2 is between 425 nm and 500 nm, the wavelength range was chosen to be able to measure SO_2 as well. In Figure 3.4 a picture of the spectrometer is shown. On either side of the spectrometer are three mounting threads in a two/one configuration. These threads are used to mount an aluminium bracket to the spectrometer, shown in Fig. 3.5. On each side, two of the

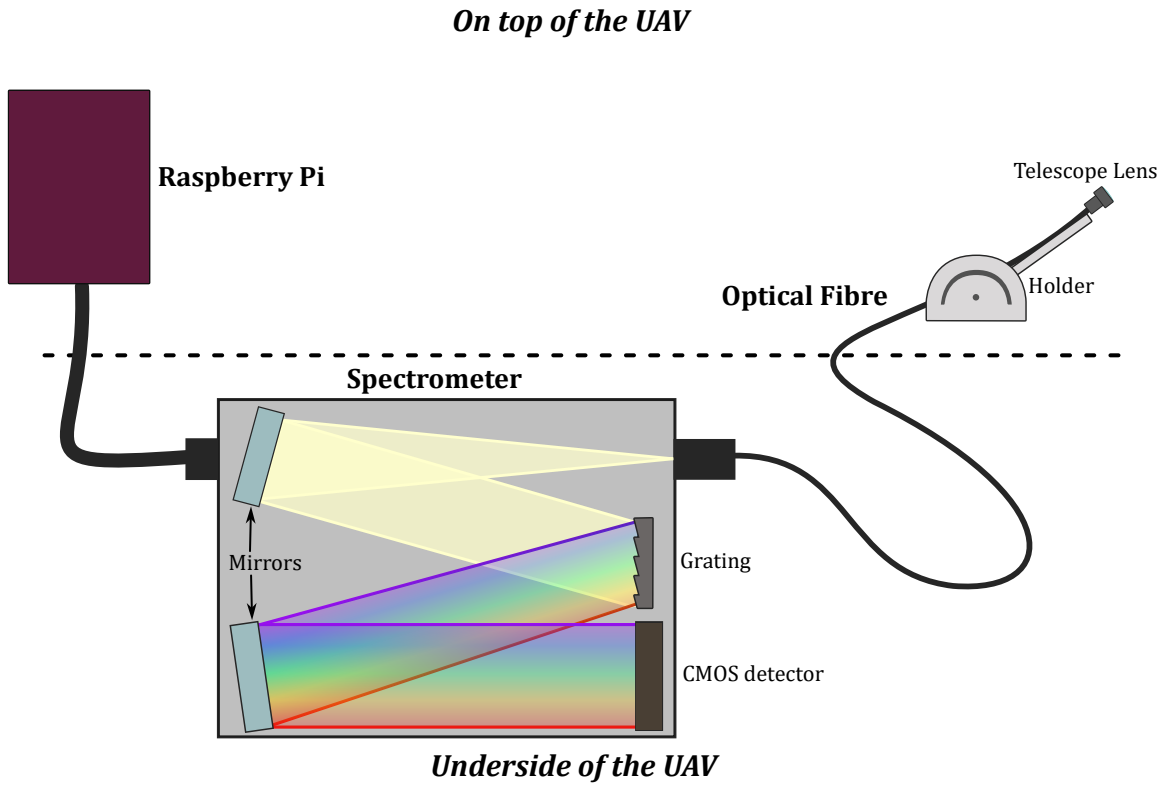


Figure 3.3: Sketch of the general DOAS setup.



Figure 3.4: A picture of the Avantes Nexos Spectrometer.

threads are used, in order to maximize the amount of screws while keeping the bracket as thin and light as possible. The bracket has a width of about 1 cm and a thickness of 4 mm. A bayonet connector made out of aluminium is positioned and fastened with

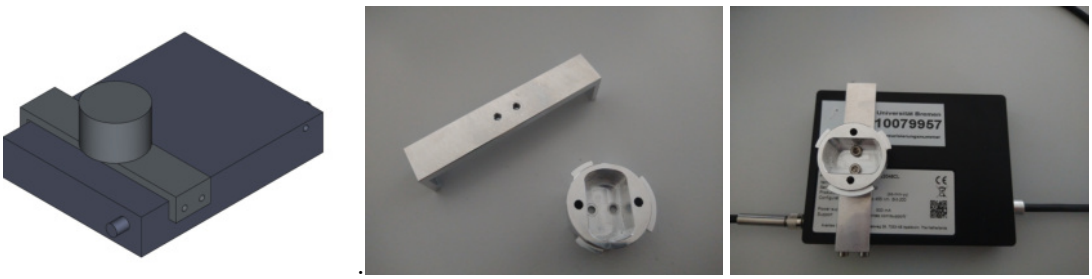


Figure 3.5: a) A 3D model of the spectrometer with bracket and simplified bayonet connector, b) finished bracket and bayonet connector, c) assembled spectrometer.

two screws on top of the bracket. The connector is used to attach the spectrometer to one of the mounts on the underside of the UAV. In total, the spectrometer mount adds 39(1) g to the payload. The mounted spectrometer is shown in Fig. 3.6.

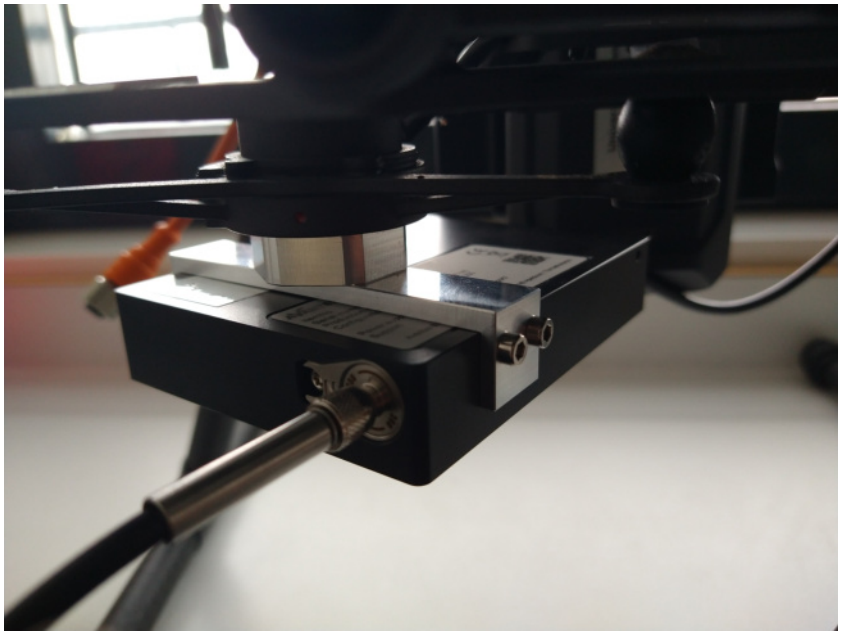


Figure 3.6: A picture of the Avantes Nexos Spectrometer mounted to the UAV using the custom-made bayonet connector and bracket.

3.2.2 The optical fibre

Since the spectrometer is on the underside of the UAV and the end of the optical fibre is mounted on top, the fibre has to be laid around the UAV. The fibre has a length of 1 m and a mass of 44(1) g. Most of the fibre is kept on the underside of the UAV, close to its body. This prevents the fibre from getting too close to the propellers during the

flight. A small telescope lens is mounted on the end of the optical fibre, as shown in Fig. 3.7. The lens has a diameter of 6 mm and a focal length of 8.7 mm. The body of the telescope can be extended to 7 mm from a minimum length of 20.5 mm to a maximum of 27.5 mm.



Figure 3.7: A picture of the telescope lens mounted on the optical fibre.

The optical fibre is not mounted directly to the measurement platform but to a holder. The holder is made out of aluminium and consists of two parts, a foot and a pole, and has a total mass of 36(1) g. Figure 3.8 shows a 3D model of the holder, the finished parts and the assembled holder.

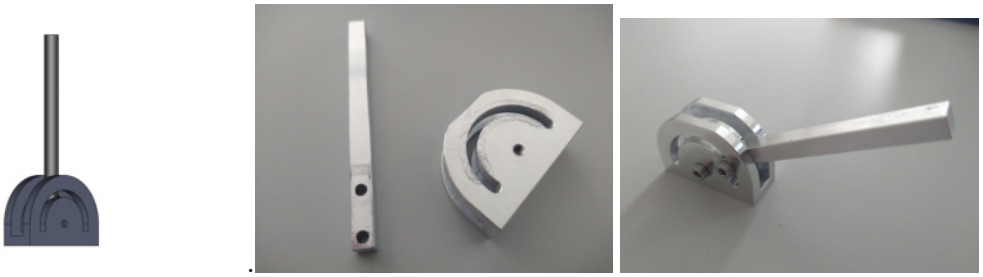


Figure 3.8: a) A 3D model of the optical fibre holder, b) the finished parts, c) the assembled fibre holder.

The foot consists of two semicircular walls with a radius of 2 cm and a width of 4 mm. The walls are about 7 mm apart and are connected at the bottom. The bottom has three holes spaced 1.5 cm apart, slightly reducing the mass of the foot, which are used to mount it to the measurement platform. The walls have two cut-outs, a hole in the center of the semicircle and a semicircular one with a radius of 1.25 cm. The cut-outs are made to fit M3-screws that hold the pole between the two walls.

The pole has a thickness of 6 mm, which is similar to the diameter of the optical fibre and prevents the pole from bending while not adding too much mass. At one end of the pole are two holes with the same distance between them, as the distance of the cut-outs of the foot. The one at the bottom is used to create an anchor point around which the pole is rotated. The other one limits the rotation of the pole to a maximum of 180° and can be used to lock the pole into position by fastening the screw tightly. This configuration allows for an easy adjustment of viewing angle of the optical fibre. However, the angle can only be adjusted between flights on the ground. Using a motorized adjustment of the viewing angle, enabling the angle to be changed mid-flight and a scanning of the plume, was not possible with this drone due to mass constraints.
The optical fibre is fastened to the top of the pole. To reduce the risk of breaking the optical fibre by over bending it, the length of the pole was set to 7 cm. Therefore, the pole can be used to perform zenith measurements at a viewing angle of 90° without straining the optical fibre. However, a longer pole poses a higher risks of the fibre colliding with the rotors.
There are multiple places on the measurement platform, where the holder could be placed. However, most of them are not suitable, because either the holder cannot be mounted securely due to cables or the telescope gets too close to the rotors, which can happen for lower viewing angles. The latter is a more general problem, since the rotor can bend up to 2 cm upwards, while the UAV is descending.



Figure 3.9: A picture of the of the optical fibre with the telescope lens mounted to the measurement platform using the fibre holder and a spacing block.

In order to be able to measure the whole angle range while avoiding the rotors, the holder is mounted higher using a 3D-printed spacing block, as shown in Fig. 3.9. The foot is mounted to the block via two screws, increasing its height by 2 cm. This allows the fibre to be orientated to point to the front of the UAV, simplifying manoeuvring.

3.3 Total payload and flight time

The UAV has a total mass of 5768(7) g with just the mandatory payload and therefore, an estimated total flight time of 26.78(7) min. Table 3.1 shows an overview of all the possible attachments of the UAV mentioned earlier and their mass-related reduction of the total flight time. The flight time is further reduced by the power consumption of the payload, which share the power provided by the batteries with the UAV.

	Mass [g]	Flight Time Reduction [min]
Measurement Platform	579(1)	4.32(1)
Avantes Nexos	265(1)	1.98(1)
Telescope Lens	5(1)	0.04(1)
Optical Fibre	44(1)	0.33(1)
Fibre Holder	36(1)	0.27(1)
Spectrometer Mount	39(1)	0.29(1)
DJI Camera X4S	251(1)	1.87(1)
Total	**1219(7)**	**9.10(7)**

Table 3.1: Overview of the mass of the payload and the mass-related reduction in flight time.

In order to measure the power consumption, the Raspberry Pi was connected to a laboratory power supply with voltages ranging from 11.0(2) V and 18.2(3) V, a similar range provided by UAV. The voltage was varied to estimate the current needed to upkeep the power requirements of the payload. Connecting only the sensors during the measurements, currents between 0.22(1) A and 0.31(1) A were observed at 15.3(3) V, which results in an average power output of 4.2(5) W. The maximum power output was measured to be 4.9(3) W. If the spectrometer is also attached to the Raspberry Pi, the needed power increased to an average of 5.90(5) W, with a maximum of 6.3(3) W. The power consumption reduces the estimated flight time by 0.20(2) min to 26.58(9) min. Thus, the mass-related flight time reduction is much more significant than the reduction caused by the power consumption of the payload.

In addition to the mandatory payload, an additional camera, a DJI X4S, can be mounted to the second bayonet connector on the underside of the UAV, which is unused. The camera allows for a 360°-view from the UAV, most importantly in the direction of the measurement, which is especially useful if it does not align with the forward direction of the UAV. Adding the camera reduces the flight time further by 1.87(1) min to a total estimated flight time of 24.7(1) min. A picture of the fully assembled UAV is shown in Figure 3.10.



Figure 3.10: Picture of the fully assembled UAV.

4 Software

The measurements are controlled by multiple Python scripts running on the Raspberry Pi. Originally, the idea was to just modify the operating system of the CRUSOE-system, but due to incompatibilities with the Avantes software, a new operating system for the Raspberry Pi was setup. The Drone-DOAS-system uses the newer Raspberry Pi OS 13 (Trixie) compared to Raspberry Pi OS 10 (Buster) used by the CRUSOE-system. Necessary scripts, that are used by the CRUSOE-system to control the pre-existing hardware, were updated to fit the drone-DOAS measurements.
During booting of the Raspberry Pi, the watchdog-script is started automatically and is running for the whole time the Raspberry Pi is switched on. The watchdog-script checks whether the Raspberry Pi is connected to a network, either wireless or by a LAN cable. If the Raspberry Pi is connected to a network, the lab mode is started and other scripts

have to be started manually. This mode is intended for calibration and test measurements, since having more control over them. If the Raspberry Pi is not connected to a network, the field mode is started. In the field mode, all necessary scripts are started automatically. The watchdog-script can also check for a monitor connected to the Raspberry Pi to display measurements.
During flights, the watchdog-script checks constantly, if the measurement scripts are still running and if necessary, restarts them. Additionally, it also controls the three status LEDs on the measurement platform, which allow for a quick assessment of measurement problems. The red LED is turned on constantly, if the Raspberry Pi has power. The yellow LED indicates the status of the watchdog-script and is turned on, if the script is running. Lastly, the green LED indicates the status of the measurements. If the LED is blinking, individual measuring devices might take faulty or no measurements. If there are no problems, the LED is constantly shining.

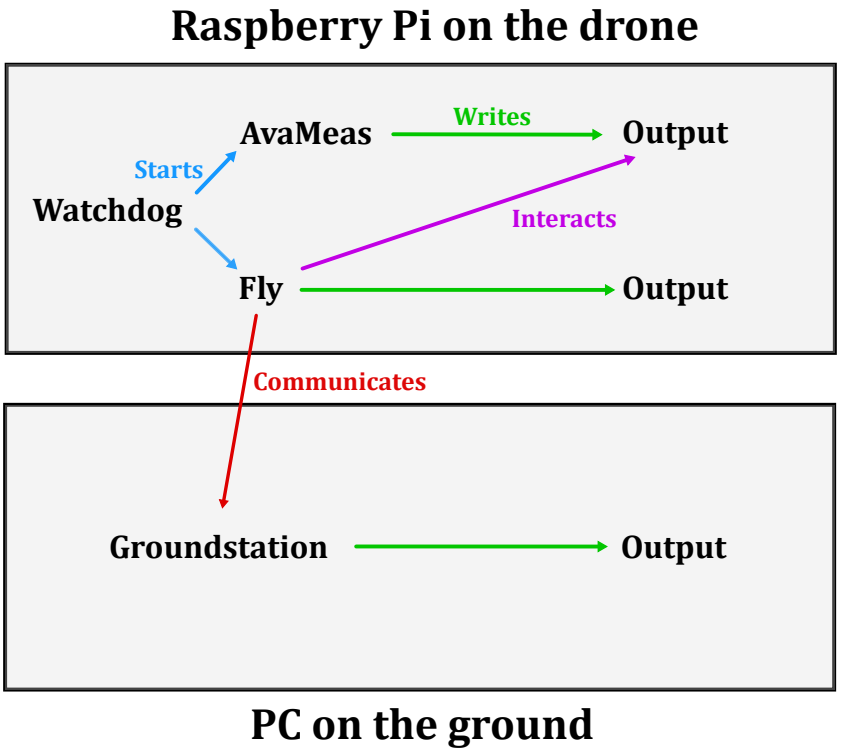


Figure 4.1: An overview of the different scripts running on the Raspberry Pi and on a computer on the ground.

Multiple other scrips run before or after the start of the UAV. A simplified overview of all scripts is shown in Fig. 4.1. If the Raspberry Pi is in the lab mode, a calibra-

tion measurement with a HgCd spectral lamp and a zenith measurement can be taken, before a flight. The measurements are performed by the scripts AvaCal and AvaRef respectively. The output is automatically saved in the correct folder, so it can be used by other scripts.
During a flight, the Raspberry Pi is in the field mode and the two measuring scripts AvaMeas and fly are started automatically. The AvaMeas-script controls the measurements of the spectrometer, using the avaspec library by Avantes. For each flight the spectra are saved in a separate file.
The fly-script reads out the measurements of all the other sensors, as well as the GPS data and orientation from the UAV. Additionally, the fly-scripts reads out the last spectrum taken by AvaMeas and a simplified DOAS-fit is conducted during the flight, using the reference and the calibration measurements. The results of the DOAS-fit, the GPS data and the measurements of the sensors are then sent by the fly-script to the PC on the ground. The read out and transfer of the data is set to be performed twice per second. In reality, only one transfer per second is performed on average, due performance limitations. As the Raspberry Pi used has just 1 GB of RAM, only essential operations are performed during a flight.
On the ground, a PC is running the groundstation-script. It receives the data sent by the UAV and saves them. The received NO_2 contents are plotted, allowing for in-flight evaluation of the results.

5 Calibration measurements

5.1 Characterization of the spectrometer

In order to assess the quality of the measurements, and since the spectrometer was never used before, the spectrometer must be characterized and calibrated. There are several aspects that have to be considered in order to describe the behaviour of the spectrometer. To do this, several measurements were performed using either a mercury-cadmium (HgCd) spectral lamp or a halogen lamp as a light source. The general setup for these measurements is already shown in Figure 3.3, although for some, different kinds of filters were placed in front the optical fibre.

5.1.1 Dark measurements

An important aspect in describing the behaviour of the spectrometer is the behaviour of the CMOS detector, especially in regard of the linearity of the measured signal. If no light source is used, the detector measures a dark current. The dark current is a background signal present in all measurements and has to be subtracted. The intensity of the dark spectrum depends on the exposure time and should increase linearly if the exposure time is increased.
To verify this, measurements of the dark spectrum of the spectrometer and of a halogen lamp were taken for different exposure times t_E.
For the dark measurements the exposure times t_E was increased from 0.025 s to 102.4 s doubling it each time. Shown in Fig. 5.1a, the intensity I, as well as the noise, of the dark spectrum increases with the exposure time t_E until it reaches saturation of 16384 Counts at 102.4 s.
Plotting the average intensity I_{avg} for each measurement against the exposure time t_E, seen in Fig. 5.1b, results in a linear relationship that can be described with $I_{\mathrm{avg}}(t_{\mathrm{E}}) = 241(5)\,\mathrm{Counts\,s^{-1}}t_{\mathrm{E}} + 28(86)\,\mathrm{Counts}$, confirming the linearity of the dark spectrum of the spectrometer.

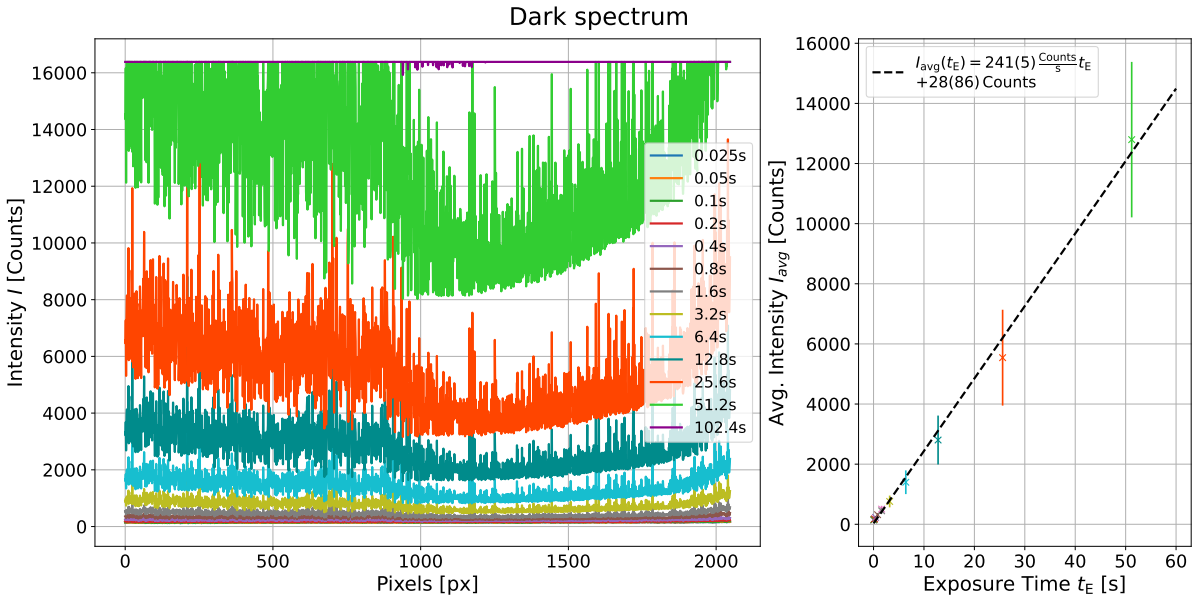


Figure 5.1: a) The dark spectrum measured with the Avantes Nexos spectrometer for different exposure times t_{E} and b) The average intensity I_{avg} of the dark spectrum over t_{E}

5.2 Linearity of the detector

For measurements with a light source, a linear increase in the light intensity should result in a linear increase of the signal read-out by the detector. Similar to the measurement of the dark signal, the spectrum of a halogen lamp was measured for exposure times t_E between 50 ms and 3000 ms, as increasing the intensity of the light source used is not possible.

The measured signal increases with t_E, although this increase is more prominent at the upper range of the detector, where the halogen lamp is more intense. Figure 5.2 shows the spectrum of the halogen lamp for the different exposure times t_E as well as the quotient of the measurement to a reference measurement with a t_E of 100 ms, displaying the ratio between the intensities I_{rat}. For the lower range of the detector, the ratio has a lot of noise due to the low signal of the halogen lamp in that area.

For the upper range of the detector, it shows that the intensity ratio I_{rat} increases similarly to the increase in exposure time t_E with a slight shifting upwards for greater t_E. The shift is probably caused by an increase in intensity of the halogen lamp during the measurements as those were done in order and would not be seen if the order of the different exposure times t_E were randomised.

To have a better overview of the linearity of different ranges of the detector, the CMOS

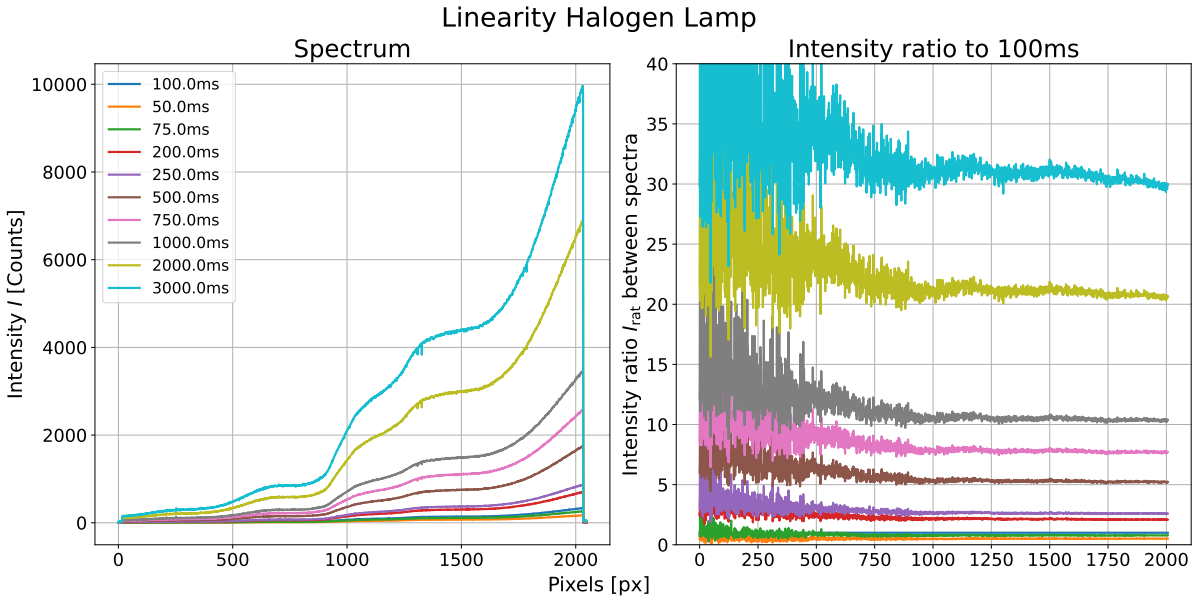


Figure 5.2: a) The spectrum of a halogen lamp for different exposure times t_E and b) the intensity ratio I_{rat} between the spectra at different exposure times t_E to a reference measurement with t_E=100 ms.

was divided into four sections, each 500 px wide. For each section, the average intensity I_{avg} was determined and plotted against the exposure time t_E, which is shown in Fig. 5.3. In each section, the detector read-out increases linearly. Due to the intensity distribution

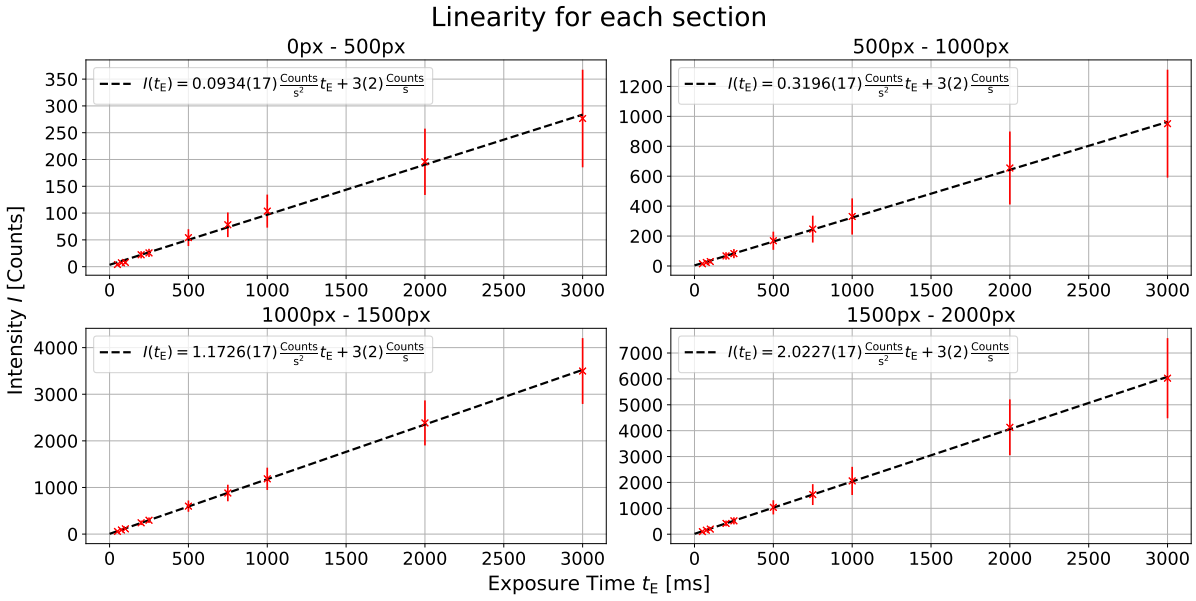


Figure 5.3: The intensity I averaged over 500 px in relation to the exposure time t_E for four sections of the CMOS detector.

of the lamp, the slope differs for each section with a minimum of $0.0934(17)\,\mathrm{Counts\,s^{-1}}$ and a maximum of $2.0227(17)\,\mathrm{Counts\,s^{-1}}$.
Since the intensity of the halogen lamp was too low in the detector range 0 px to 500 px, a spectrum of a HgCd lamp was measured as well. As shown in Fig. 5.4, the HgCd lamp has four peaks in that range of the detector. For every measured exposure time t_E, the

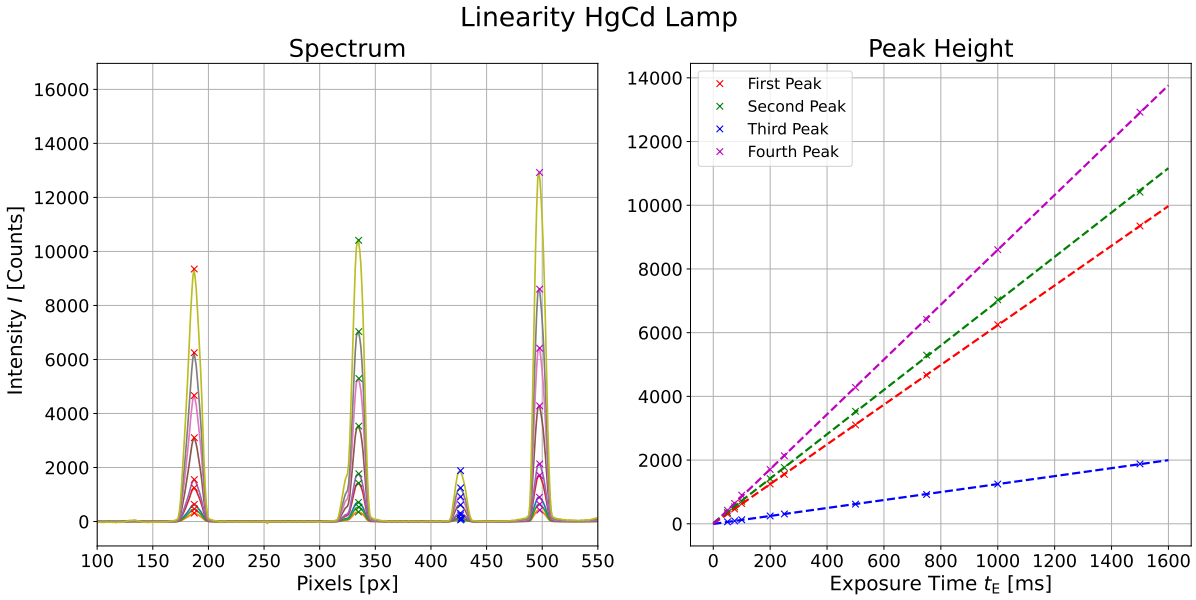


Figure 5.4: a) Four peaks of the spectrum of a HgCd lamp for different exposure times t_E and b) the intensity I of the four peaks over the exposure time t_E.

intensity I of each peak was determined and plotted. This shows again a linear relation between the measured signal and the exposure time t_E confirming the measurement with the halogen lamp in the lower detector range.
Therefore, the signal read-out of the CMOS detector of the spectrometer increases linearly with a linear increase of the light intensity.

5.2.1 Calibration using a HgCd lamp

The spectrum is measured with the pixels of the CMOS detector of the spectrometer and therefore, has to be calibrated to the wavelength. According to the manufacturer, the spectrometer has a wavelength range of 300 nm to 450 nm and a full width at half maximum (FWHM) of 1.6 nm. For the calibration a HgCd lamp is used as its spectrum has 8 sharp peaks in this wavelength range, seen in Fig. 5.5a. The peaks have wavelengths λ of 313.3167 nm, 326.1055 nm, 340.3652 nm, 346.62 nm, 361.0508 nm, 365.0153 nm, 404.6563 nm, and 435.8328 nm. To determine a more precise position of

the peaks, the spectrum is interpolated. As also seen in Fig. 5.5b, the relation between the wavelength λ and the pixel position of the peak can be described with a third-degree polynomial

$$\begin{aligned}\lambda(px) = &-8.6(13) \cdot 10^{-10} \frac{\text{nm}}{\text{px}^3} px^3 - 2.9(3) \cdot 10^{-6} \frac{\text{nm}}{\text{px}^2} px^2 \\ &+ 8.975(29) \cdot 10^{-2} \frac{\text{nm}}{\text{px}} px + 296.36(6)\,\text{nm}.\end{aligned}$$

Therefore, the spectrometer has a wavelength range of 296 nm to 460 nm, which is in accordance with the manufacturer's specifications. This relationship will be used to calibrate the spectrometer.

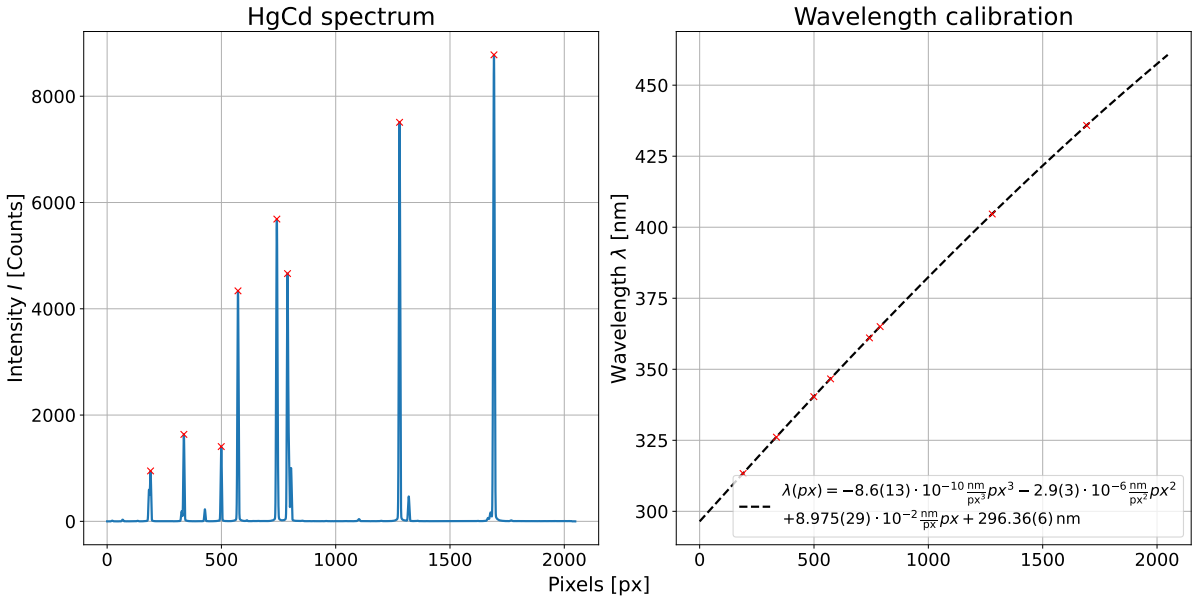


Figure 5.5: a) The full spectrum of a HgCd lamp measurable with the spectrometer and b) the relation of the peaks of the HgCd lamp and their position on the CMOS detector.

Another important aspect, is the full width at half maximum (FWHM) of the peaks,which are used to determine the slit function of the spectrometer, which is used when comparing the spectra of two different spectrometers. The peaks of the actual spectrum of a spectral lamp would be described by delta-functions, however due to the finite size of the components of the spectrometer, the peaks have a finite width. Therefore, the measured spectrum is a convolution of the actual spectrum and the spectrometer-specific slit function.
The peaks of the HgCd lamp can be approximated with a Gauss-function $g(x) =$

$a \exp\left[-b(x-x_0)^2\right] - c$, as seen in Fig. 5.6. These Gauss-functions can be used to calculate the FWHM of the peaks with $FWHM = 2\sqrt{\frac{\ln 2}{b}}$.

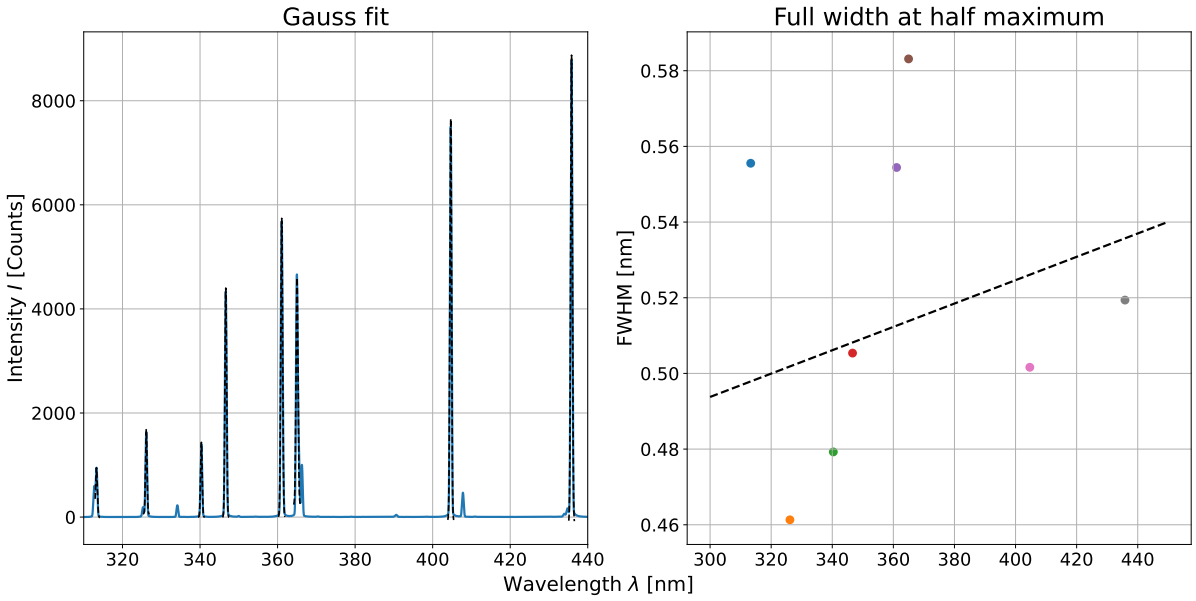


Figure 5.6: a) the spectrum of the HgCd lamp calibrated to the wavelength λ and fitted with Gauss-functions and b) the calculated FWHM for the different peaks over the wavelength λ.

The calculated FWHMs range between 0.46131(13) nm and 0.5831(9) nm. Generally, it is expected that the FWHM increases with the wavelength λ, however for this, only a slight tendency is seen. All determined FWHMs are smaller than the value specified by the manufacturer.

5.2.2 Temperature dependency

The measurements with the Drone-DOAS system can be performed at temperatures between -10 °C and 40 °C. A change in temperature of the spectrometer can shift where light with a specific wavelength hits the detector. Since the temperature cannot be held constant during the flight, the temperature dependency of the spectrometer has to be characterized.

To measure the temperature T, the Bosch BMP388 and Sensirion SHT31-DIS of the base plate are used. The measurements were done at a room temperature T_R of 19 °C and the sensors and the spectrometer were either cooled to a minimal temperature $T_{\min}$ of 15.7(3) °C by opening a window or heated to a maximum temperature $T_{\max}$ of 26.3(3) °C by using a halogen lamp. The temperatures measured by the different sensors deviate

slightly, either due to a different distance to the window and lamp or due to differences in the way these measure the temperature. Therefore, the temperature measured by the Sensirion SHT31-DIS is used for the characterization, as this sensor is primarily used to measure the temperature.
For the measurements, the spectrum of the HgCd lamp was used to determine the dependency on temperature. The HgCd lamp was placed far enough away from the window and halogen lamp so, that the effects of the temperature change to the HgCd lamp are negligible. The shift in temperature T causes the positions of the peaks on the CMOS detector to shift. Figure 5.7 shows the shift ΔPX in pixels of the peak position compared to referenced measurement taken at room temperature T_R beforehand, as well as the converted shift in units of wavelength $\Delta\lambda$.

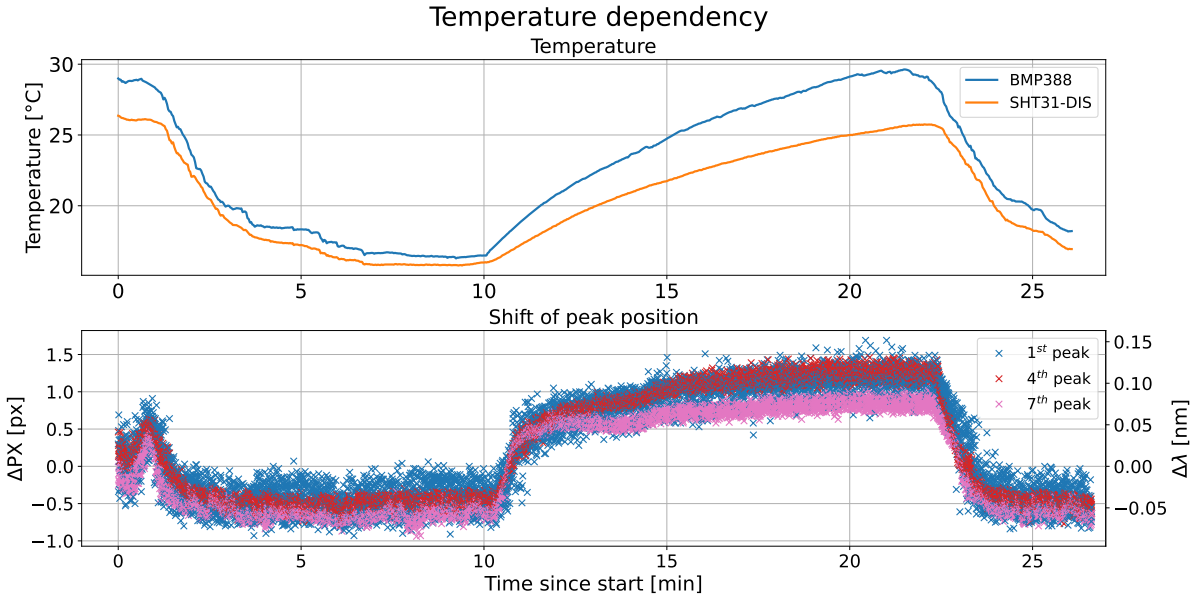


Figure 5.7: Top: The temperature T over the course of the measurement using the Bosch BMP388 and Sensirion SHT31-DIS sensors. Bottom: The shift ΔPX and $\Delta\lambda$ of the 1st, 4th and 7th peak of a HgCd lamp over the time of the measurement.

Using the wavelength calibration determined before, the measured peaks shift toward shorter wavelengths, if the temperature T decreases and toward longer wavelengths, if the temperature increases. In total, the peaks shift by about 0.15(2) nm in the measured temperature range ΔT of 10.6(6) K resulting in a change rate

$$\Delta_\lambda = \frac{\Delta\lambda}{\Delta T}$$

of $0.014(2)\,\mathrm{nm\,K^{-1}}$, or a rate Δ_{px} of $0.14(2)\,\mathrm{px\,K^{-1}}$. This means over the whole temperature range, the spectrum is expected to shift by $0.7(2)\,\mathrm{nm}$ or $7(2)\,\mathrm{px}$, if the shift is linear.

5.2.3 Straylight

Another aspect, that has to be characterized, is the possibility of straylight within the spectrometer, which is caused by randomly scattered light hitting the detector. The spectrum of a halogen lamp is measured with different optical filters in the light path. The filters have cut-off wavelengths between 340 nm and 460 nm and absorb all light with wavelengths shorter than the cut-off wavelength and only longer ones get transmitted. Measurements without an optical filter were taken before and after the series of measurements with the filters, with the latter used as reference. During the measurements, the intensity of the halogen lamp slightly increased. However, the increase is insignificant for the rest of the measurements. For the halogen lamp, the spectra are shown in Fig. 5.8, with the vertical lines indicating the wavelengths of the optical filters. Compared to the reference measurements, the spectra of the measurements with a filter become slowly less intense around the filtered wavelength λ. The measurements with the Y400, Y420 and Y460 filters show an increase in intensity in the range between 375 nm and 425 nm, that could be caused by stray light.

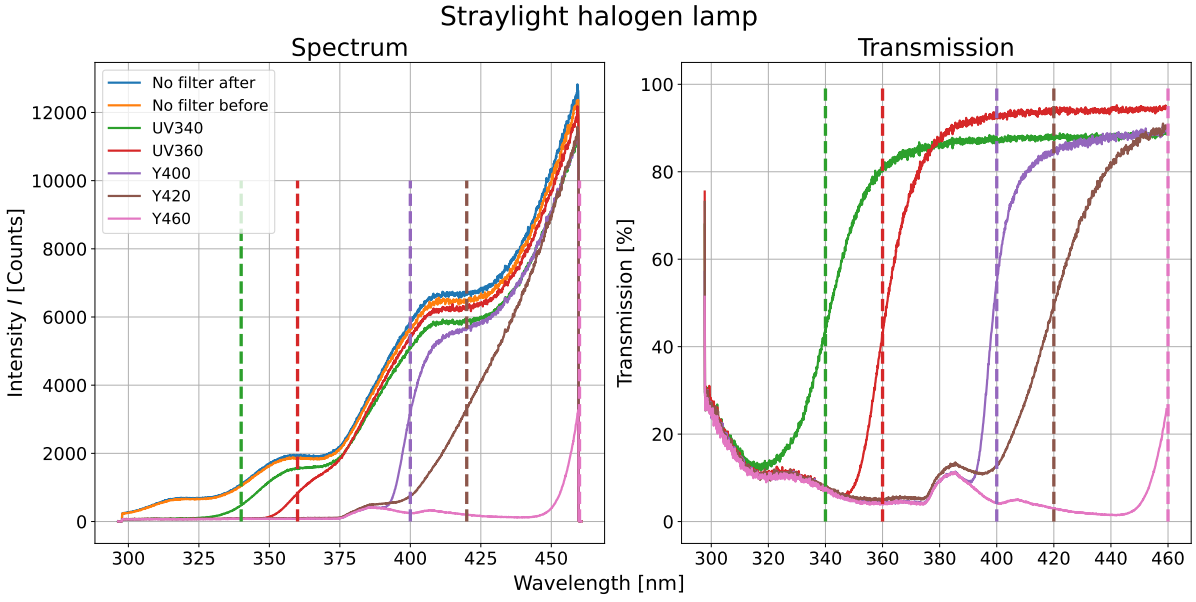


Figure 5.8: a) The spectrum of a halogen lamp while using different optical filters and b) the transmittance of the spectrum with the optical filters in percent over the wavelength λ.

The quotient of a filtered measurement and the reference show the percentage of light that is transmitted by the filters. The filters have a near vertical absorption curve with the cut-off wavelength as turning point. These curves have a full width between 44(2) nm for the Y400 filter and 57(2) nm for the Y420 filter, which is larger than expected and explains the slow decrease in intensity of the spectra. For the measurement with the Y460 filter, the transmittance has a minimum of 2 %, otherwise, a minimum of 5 % was measured. The transmittance has a local maximum of 10 % at 385 nm, coinciding with the increase in intensity of the spectra, and increases for wavelength shorter than 345 nm to a maximum of 30 %. Possible causes for this are the low intensity of the halogen lamp in the UV, the insufficient transmittance of the optical filters, or straylight.
The measurements were repeated with the HgCd lamp, shown in Fig. 5.9, to test the transmittance of the filters.

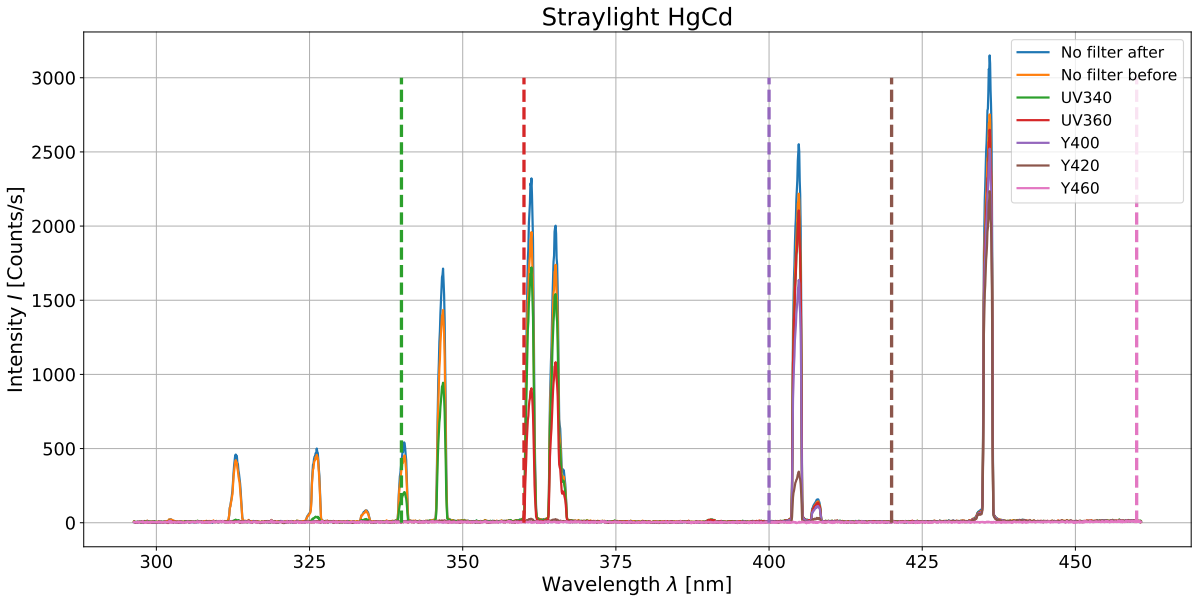


Figure 5.9: Spectra of a HgCd lamp for different optical filters.

It can be seen, that the intensity of the peaks decreases below and slightly above the cut-off wavelength. Any signal measured in the filtered range coincides with a peak of the HgCd lamp, confirming the insufficient transmittance of the optical filters. HgCd lamp has a few discrete peaks in the visible range and therefore, no straylight is seen between the peaks.
In contrast, the light of the halogen lamp is mostly in the visible and a lot of light can possibly be scattered onto the CMOS detector, that is not absorbed by the optical filters. Therefore, the increase in intensity is caused by straylight, which can significantly

impact the measurements. However, most straylight hits the detector in the wavelength range below 425 nm. For the measurement of NO_2, which absorbs at longer wavelength, the influence of straylight is negligible. If SO_2 is to be measured, a sufficient filter for wavelengths above the measurable range would have to be implemented.

5.2.4 Polarization

It is possible that the spectrometer has a different sensitivity to different polarization states of the incoming light. The light of a halogen lamp or the sun are unpolarized. However, the measured sun light is Rayleigh scattered, which polarizes the light. Additionally, due to the non-polarization-maintaining fibre, the polarization state can change unpredictably leading to potential differences the measured intensity I. It is to be expected, that the measured intensity of light with a polarization perpendicular to the orientation of the slit of the spectrometer should be lower than of light with a parallel polarization state. Since the fibre is non-polarization maintaining, this tendency should be less significant.

To characterize the sensitivity of the spectrometer and the influence of the optical fibre, the spectrum of a halogen lamp was measured with a linear polarization filter directly in front of the entry of the optical fibre or directly in front of the spectrometer. The linear polarization filter absorbs any light polarized perpendicular to the angle of the filter. The angle θ of the polarization filter was changed in either 2° or 10° increments. The measurement taken at an angle θ of 0(1)° was used as a reference intensity I_0. This measurement was conducted twice and the intensity ratios $\frac{I}{I_0}$ for both measurements are shown in Fig. 5.10.

The measurements differ from the expectation, as well as from each other. In the first one, the measurements without the optical fibre seem to resemble a sine curve until an angle θ of about 100(1)°. The curve has a maximum of 2.43(12), as well as two minima at 15(1)° and 95(1)° with intensities I of 0.40(2). For angles θ over 100.0(5)° the ratio $\frac{I}{I_0}$ is more constant and fluctuates between 0.1 and 0.2. For the measurements with the optical fibre, the intensity ratio $\frac{I}{I_0}$ is roughly constant at around a ratio 1, with only small fluctuation and a minimum of 0.81(4) at an angle θ of 190(1)°. With an optical fibre, light consistently enters the spectrometer at the same angle of incident no matter where the light is coming from. Removing the fibre, this constancy is not given anymore, thus, slight movement of the filter and the spectrometer during the series of measurements probably caused the significant differences in intensity.

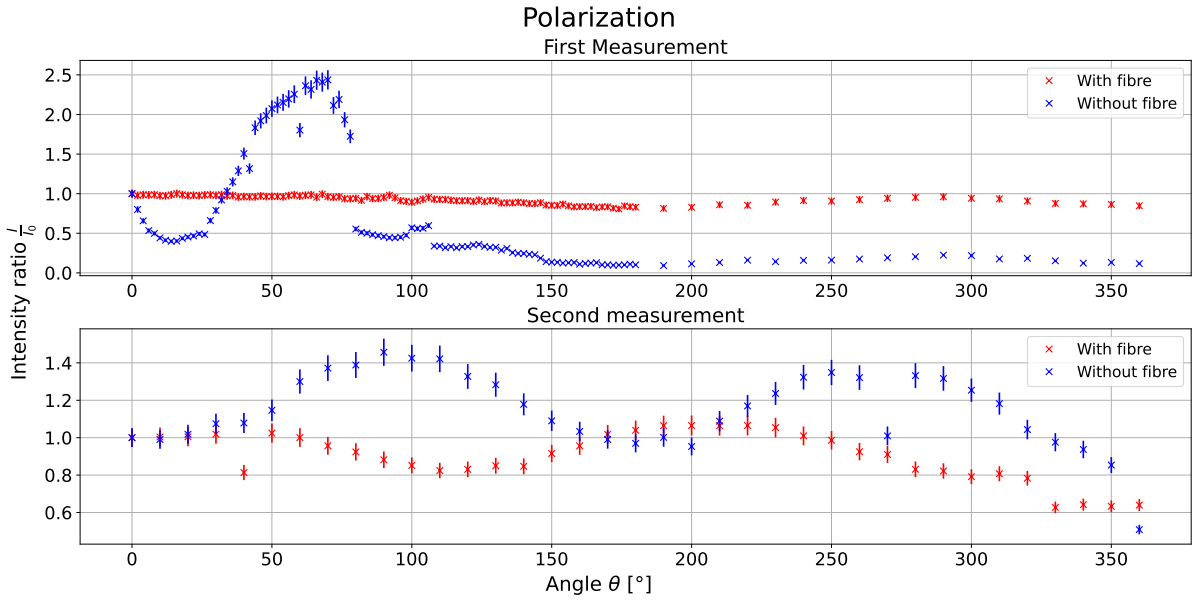


Figure 5.10: The intensity ratio $\frac{I}{I_0}$ for different angles θ of the polarization filter with and without the optical fibre attached to the spectrometer for two different measurements.

The second round of measurements was done more carefully. For these measurement series, both the measurements with and without the fibre resemble sine curves, although with a phase shift of 90 °. Without the fibre, the curve has two maxima at angles θ of 90(1) ° and 270(1) ° with a maximum intensity ratio $\frac{I}{I_0}$ of 1.46(7). A minimum was measured at 180.0(5) ° with an $\frac{I}{I_0}$ of 0.97(4). With a fibre, these maxima were located at angles θ of 45(1) ° and 225(1) °. The Intensity ratio $\frac{I}{I_0}$ for this series of measurements has a maximum of 1.07(5) and a minimum of 0.81(4). For the last four angles θ, $\frac{I}{I_0}$ drops to around 0.6, probably caused by the setup rather the polarization of the light. This is also seen for the measurements without the fibre, where the ratio has a value of only 0.51(3) measured at an angle of 360(1) °.
Thus, the measurements of the polarization are not conclusive enough to make an assessment of the sensitivity of the spectrometer itself. However, since the changes in intensity are much smaller for the measurements with the optical fibre for both series of measurements, the polarization state of the light does not influence the measured intensities significantly.

5.3 Calibration of the telescope lens

A lens is placed at the end of the optical fibre to limit the field of view. Ideally, for the DOAS measurements, the beam entering the optical fibre is as parallel as possible. As discussed in Sect. 2.3.1, this is achieved if the focal point of the lens coincides with the entry of the optical fibre. However, due to the finite size of the optical fibre, some divergence will always occur. Therefore, the lens has to be calibrated in order to yield optimal results.

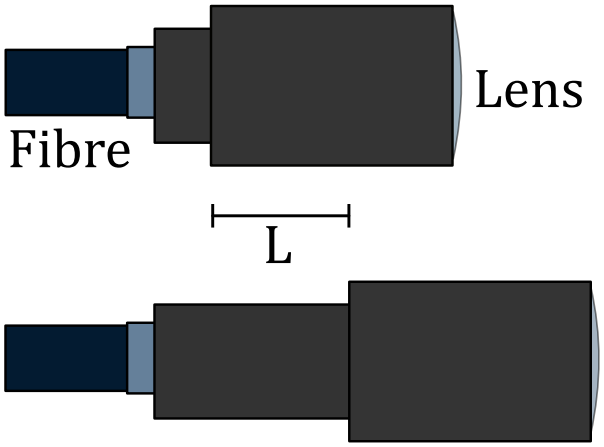


Figure 5.11: A sketch showing the extension L of the telescope lens.

The actual lens is located about 18 mm from the end of the lens body, which is attached to the optical fibre. The optical fibre itself extends about 10 mm beyond the threading, thus, the ideal adjustment of the telescope lens should be at around 0.7 mm given the focal length of 8.7 mm. To test this, light was shone through the end of the optical fibre, which is normally attached to the spectrometer. The radius r of the decoupled light beam at different distances d to the lens was measured for several extensions of the body length L. Figure 5.11 shows a sketch explaining the extension L of the telescope lens.

As a reference, the radius r of the decoupled light beam without the telescope lens in the light path was measured. Without the lens, the light beam has a radius r of 1.10(25) mm at an distance d of 2(1) mm. The radius r increases linearly to 7.40(25) mm at an distance d of 21(1) mm before it gets too diffuse and faint to be measured. An increase in r of 6.3(5) mm over a distance of 18(2) mm results in an maximum angle of acceptance $\alpha_{\mathrm{max,a}}$ of 19.29(3)° and an numerical aperture NA of 0.33(3).

For the measurements with the lens, the body was initially extended in rough increments

of about 1 mm. For all extensions L, the measured light beam resembled Gaussian beams with a small waist in the near field at a distance d between 10(1) mm and 60(1) mm. In the far field, the beam radius r increases linearly, as seen in Fig. 5.12. This shows, that the beam waist ω_0 and the Rayleigh length z_0 decrease as the extension of the lens gets longer resulting in a larger divergence angle θ. At a maximum extension of 7.0(1),mm, the beam has a waist width of 0.12(5) mm and a Rayleigh length of 1.3(9) mm. The beam diverges with an angle θ of 5.3(7)°, improving the numerical aperture to NA=0.10(7). Therefore, even a badly adjusted telescope lens yields better results than no lens at all. In general for a length L of the lens over 2.0(1) mm, the beam also got too diffuse and r could not be measured for distances d larger than 100 mm.
As expected, the best results of the rough adjustment were achieved at an extension L of 0.0(1) mm and 1.0(1) mm. For these, the radius r of the beam could still be measured at a distance d of 1.33(1) m. The beams have a larger waist ω_0 of 2.43(7) mm and 1.19(7) mm, respectively, as well as much larger Rayleigh lengths of 141(6) mm and 82(5) mm. With these, the beams only have divergence angles θ of 0.9839(12)° and 0.8333(18)°.

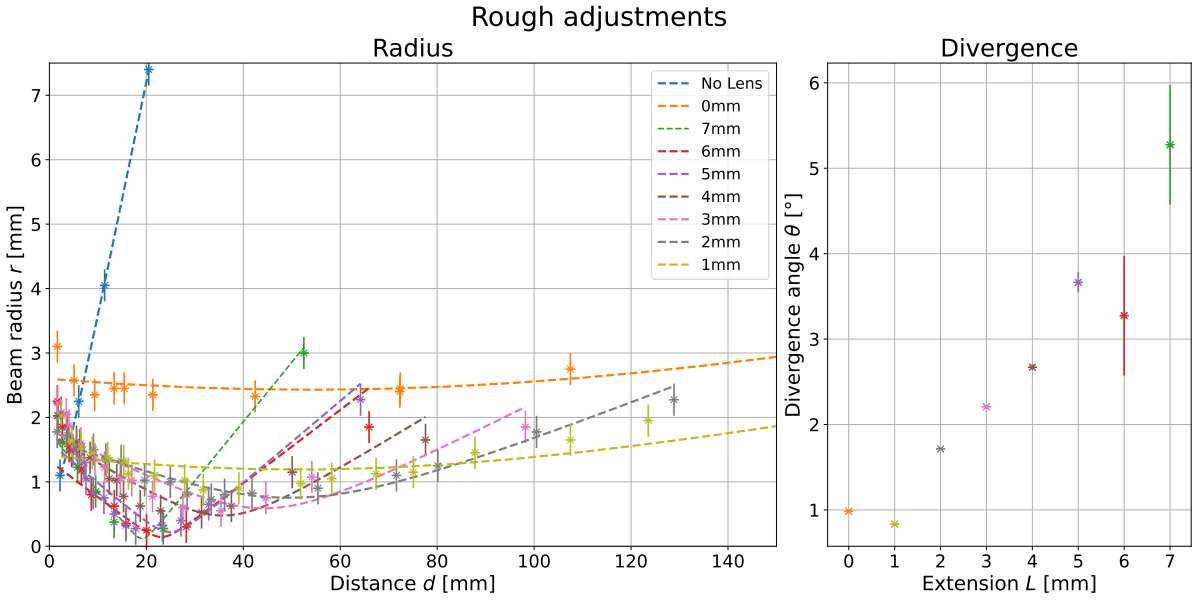


Figure 5.12: a) The measured beam radius r at different distances D for the rough adjustment of the lens and b) the determined divergence angle θ of the beams for different extensions L of the telescope lens.

Besides the rough adjustment, some finer adjustments were attempted for an extension L of the lens body between 0.0(1) mm and 1.0(1) mm. The fine adjustments were done in increments of 0.2 mm. The results are shown in Fig. 5.13.

A minimum beam waist ω_0 of 0.91(5) mm was measured at an extension L of 0.8(1) mm, which, with a Rayleigh length z_0 of 44(5) mm, results in a divergence angle θ of 1.179(3)°. ω_0 was the widest at an extension of 0.2 mm with a value of 1.48(4) mm. This corresponds to a θ of 0.996(3)°. For the other measured extensions L of the telescope lens, the divergence angle θ lies between these two values. However, the minimal divergence angle determined with the rough adjustments could not be reproduced.

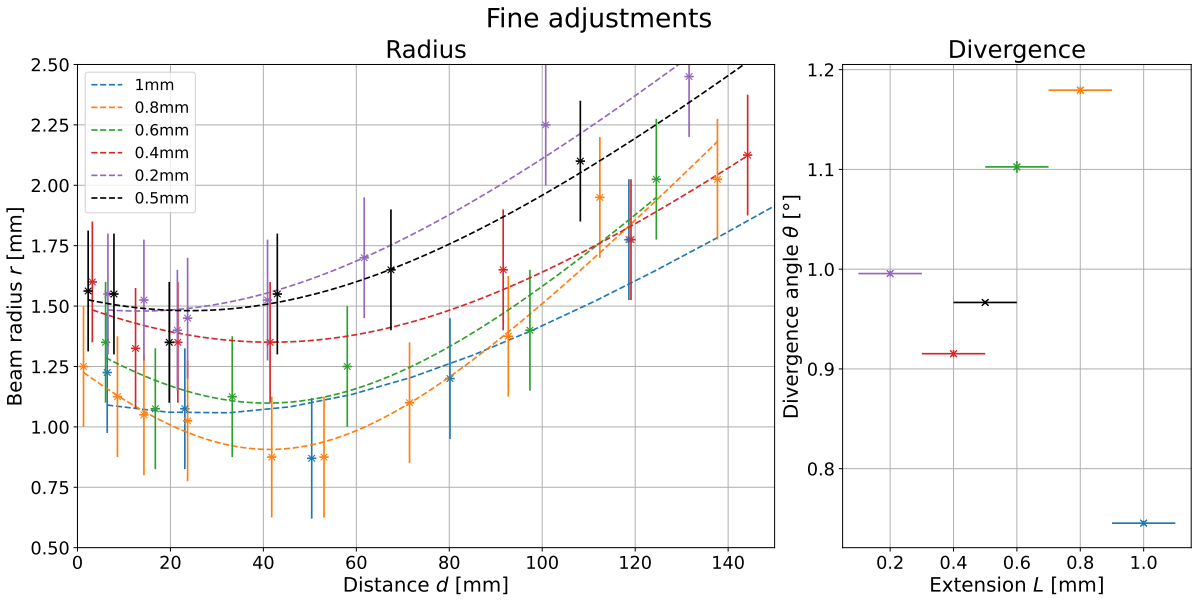


Figure 5.13: a) The measured beam radius r at different distances D for the fine adjustment of the lens b) the determined divergence angle θ of the beams for different extensions L of the telescope lens.

Due to the small size of the lens and therefore difficult and uncertain measurement, the final length L_{set} was set by slowly increasing the length L of the telescope lens until the radius r was minimal in the far field. This was achieved at an extension of L=0.5(1) mm with a radius r of 26.8(2) mm at a distance d of 1.73(1) m. With a beam waist ω_0 of 1.48(7) mm and a Rayleigh length z_0 of 87(4) mm, the beam diverges with an angle θ of 0.9666(17) ° resulting in a numerical aperture NA of 0.0169(17).

5.4 Angle calibration

The viewing angle of the optical fibre can only be set manually before the flight. Due to the form of the fibre, it is not always certain that the angle of the holder and the fibre match, rendering it difficult to measure the exact angle in the field. However, it

is important to know the angle of incidence for a given flight in order to determine the height of the plume. Multiple angles were, therefore, calibrated beforehand.
To calibrate the angle, a height-adjustable lamp was placed at a distance d from the UAV. The height of the lamp h_{lamp}, at which the maximum intensity I_{max} is measured, consists of a base height h_{base} and the adjustable height h_{adj}. The height h_{adj} can range between 0 cm and 35 cm. The UAV was standing on the ground and therefore, the measurement platform sits at a height h_{UAV} of 32.0(1) cm. The optical fibre with the telescope lens was placed similar to typical flight conditions. For the determination of the angle, the height of the lens h_{lens} has to be known. To have a reference point that can easily be measured for different angles, the center of the lens was chosen, its height h_{center} from the measurement platform is added to h_{UAV}. The angle α of the fibre can then be determined using

$$\alpha = \arctan\left(\frac{\Delta h}{d}\right)$$

with $\Delta h = h_{\text{lamp}} - h_{\text{lens}}$ as the height difference between lens and light source.
As a first measurement, the viability of the calibration was tested. For this, the fibre was set to an angle α_{est} of about 10°, as shown in Fig. 5.14, corresponding to a height h_{center} of 5.1(1) cm. The light source was placed 260(1) cm from the lens with a base

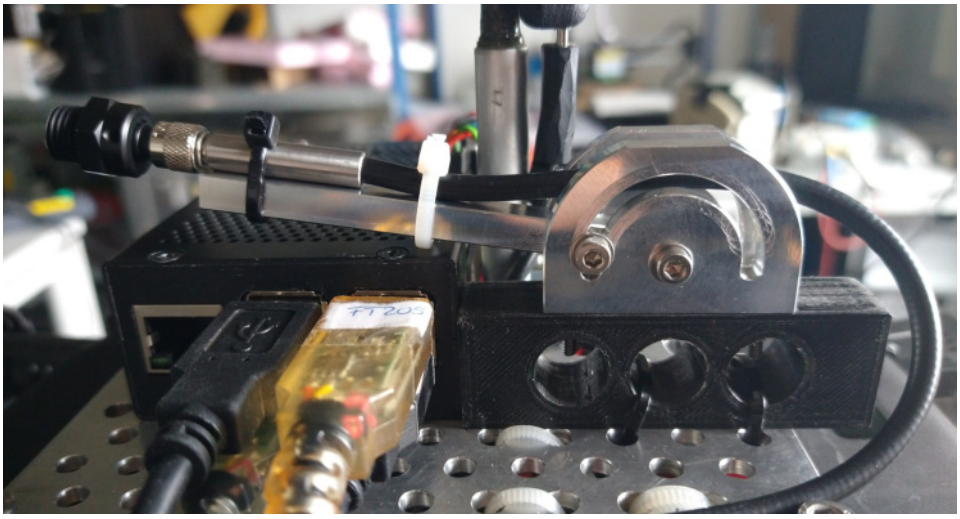


Figure 5.14: Picture of the angle of the optical fibre for the test calibration.

height h_{base} of 52.5(1) cm. h_{adj} was increased in 1 cm increments until the maximum height was reached. At each height, multiple measurements were taken and averaged to account for the slight instability of the lamp. Figure 5.15 shows the maximum intensity

I_{max} for each height h_{adj}. The highest intensity was measured at a height h_{adj} between

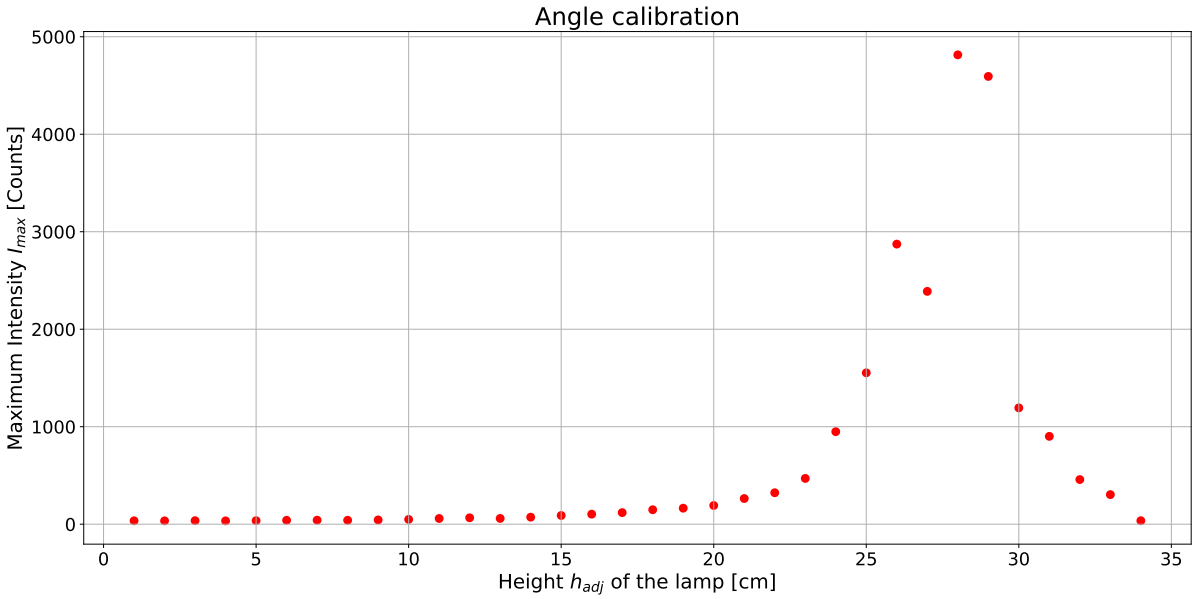


Figure 5.15: The maximum intensity I_{max} measured at different heights h_{adj} of the light source.

28 cm and 29 cm resulting in a total height h_{lamp} of about 81.0(6) cm. This gives an angle α of 9.584(4)°, which is close to the estimation α_{est} of 10°.
The placement of the optical fibre on the pole of the holder is easily reproducible. Therefore, a calibration was performed for four different viewing angles in total. For these measurements the height of the light source was increased continuously and the maximum intensity I_{max} was observed simultaneously with a special version of the groundstation-script. The measurement for the first angle α is illustrated in Figure 5.16. The angle α chosen is the lowest angle that can be used for measurements for this placement of the fibre.

For this measurement, the distance d between lamp and lens was 230(1) cm and the heights h_{base} and h_{center} were 42.8(1) cm and 4.6(1) cm respectively. In the first few minutes, the height h_{adj} was slowly increased. At around six minutes, h_{adj} was increased and subsequently decreased more rapidly in order to find a rough estimate of the needed height. Afterwards, h_{adj} was slightly changed around the rough estimate to determine the height of the maximum intensity. At the end of the measurement, the height was shortly increased again to confirm the maximum. In the end, a maximum intensity I_{max} was measured at a height h_{adj} of 16.3(1) cm resulting in an angle α of 5.575(2)°. Using this method, four angles between 5° and 30° were determined, for more details see

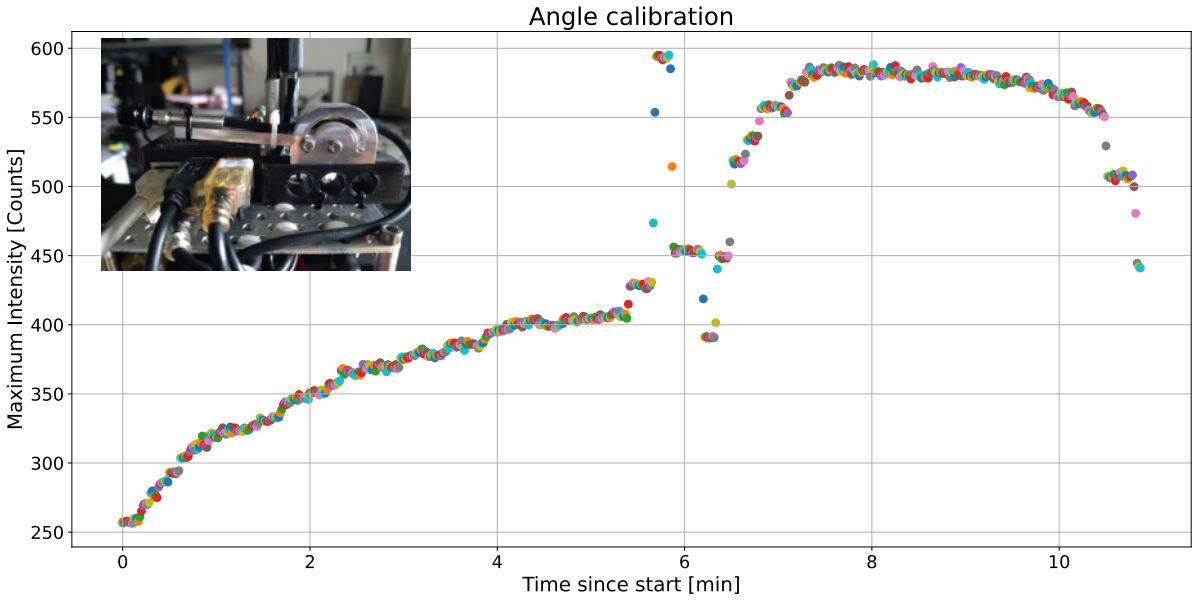


Figure 5.16: An example of the angle calibration. The maximum Intensity $I_{\max}$ was measured over time while the height of the light source was adjusted. Inset: Picture of the angle of the optical fibre.

Tab. 5.1.

In order to be able to set the viewing angle in the field, they were marked in the foot of the optical fibre holder, shown in Fig. 5.17. For the angle to be correctly adjusted, the top of the pole has to match with the marked line.

Distance d [cm]	Height lamp h_{lamp} [cm]	Height lens h_{lens} [cm]	Angle α [°]
230(1)	59.1(2)	36.6(2)	5.575(2)
351(1)	103.2(2)	37.2(2)	10.649(2)
351(1)	141.1(2)	38.7(2)	16.264(3)
236(1)	170.2(2)	40.8(2)	28.736(4)

Table 5.1: An Overview of the distance d between the lamp and the lens, the total height of the lamp h_{lamp}, the total height of the lens h_{lens} and the calculated viewing angle α of the optical fibre.

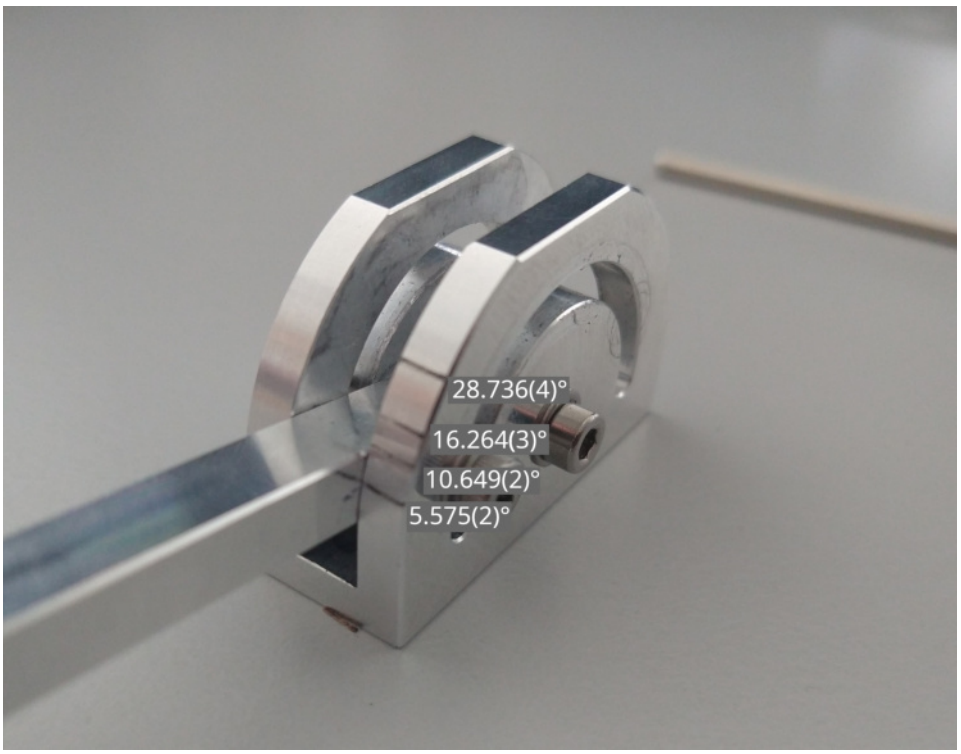


Figure 5.17: The optical fibre holder with the marks for the four angles 5.575(2)°, 10.649(2)°, 16.264(3)° and 28.736(4)°. In the picture, the holder is set to 10.649(2)°.

6 Test measurements

Before a flight, two aspects of the measurement system had to be tested. On one hand, the long-term stability of the spectrometer is important to further quantify the quality of the measured spectra. On the other hand, it is important to test the software. While some parts of the software were already used for the characterization measurements and thus, were already known to be working properly, the software has to be tested in conditions similar to a flight.

6.1 Tests with an NO_2 cell

During a flight, multiple scripts have to run and interact with each other to ensure all data is saved correctly and first results can be seen in near-real-time. Most important part to test is the simplified DOAS-fit performed by the fly script on the Raspberry Pi and the displaying of the results on the groundstation. The measurements use an NO_2 cell, a small cylinder filled with NO_2, to simulate different slant columns SC.

The simplified DOAS-fit works by calculating the optical thickness D according to Eq. (2.3.12a), using a measurement without the NO_2 cell in the light path as the reference $I_0(\lambda)$ and a measurement with the NO_2 cell as $I(\lambda)$. Both spectra, as well as the calculated optical density D, can be seen in Fig. 6.1.

Using the normalized absorption cross-section $\sigma_{NO_2}(\lambda)$ (Vandaele et al. 1998), D can

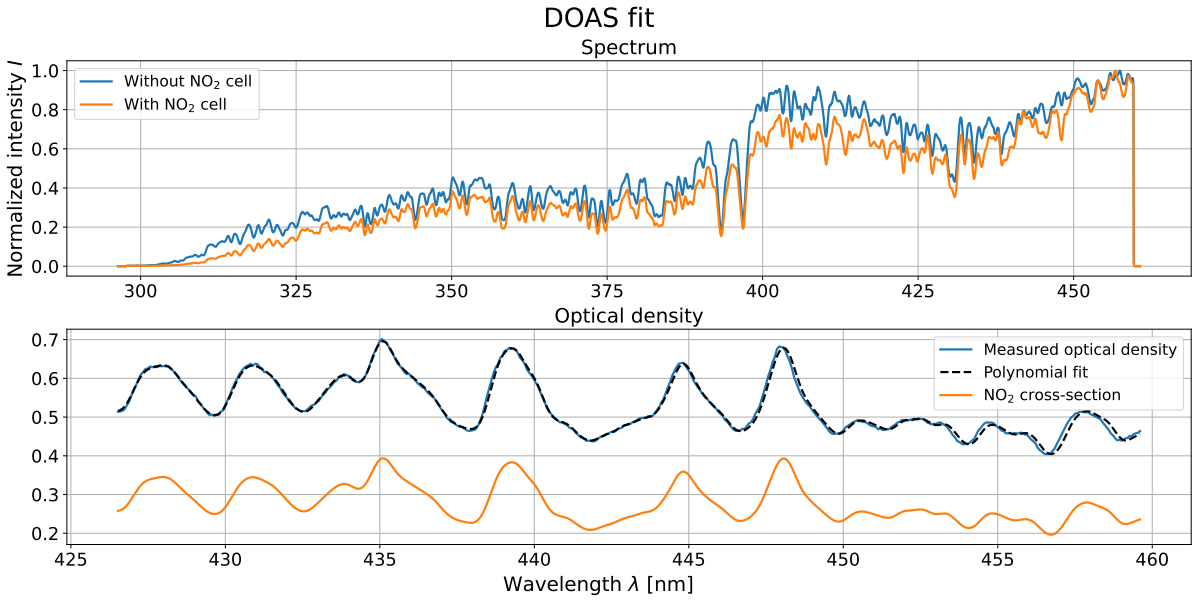


Figure 6.1: Top: A spectrum measured with and without the NO_2 in the light path. Bottom: The determined optical density D of the two spectra with the NO_2 cross-section σ_{NO_2} used for the non-linear fit.

be fitted with the polynomial fit

$$D(\lambda) = c_4\lambda^4 + c_3\lambda^3 + c_2\lambda^2 + c_1\lambda + c_0 + SC\sigma_{NO_2}(\lambda) \tag{6.1.1}$$

The last term of the fit gives a slant column SC of $1.343(8)\cdot10^{18}\,\mathrm{molec\,cm^{-3}}$, which gets transmitted to the groundstation. This process is then repeated for all spectra measured.

In order to simulate a change in the NO_2 content, the cell was held in front of the telescope lens and tilted in different directions to change the path length L through the cell. Figure 6.2 shows the measured NO_2 slant column SC over the time t. The plot corresponds to one of the plots displayed by the groundstation during a flight.

When the NO_2 cell is placed in the light path, a significant increase in the NO_2 content can be observed. Initially, this increases to $1.344(8)\cdot10^{18}$ molec $\mathrm{m^{-3}}$. Due to the photolysis of NO_2 into NO and O, the NO_2 content in the cell decreases to $1.208(8)\cdot10^{18}$ molec

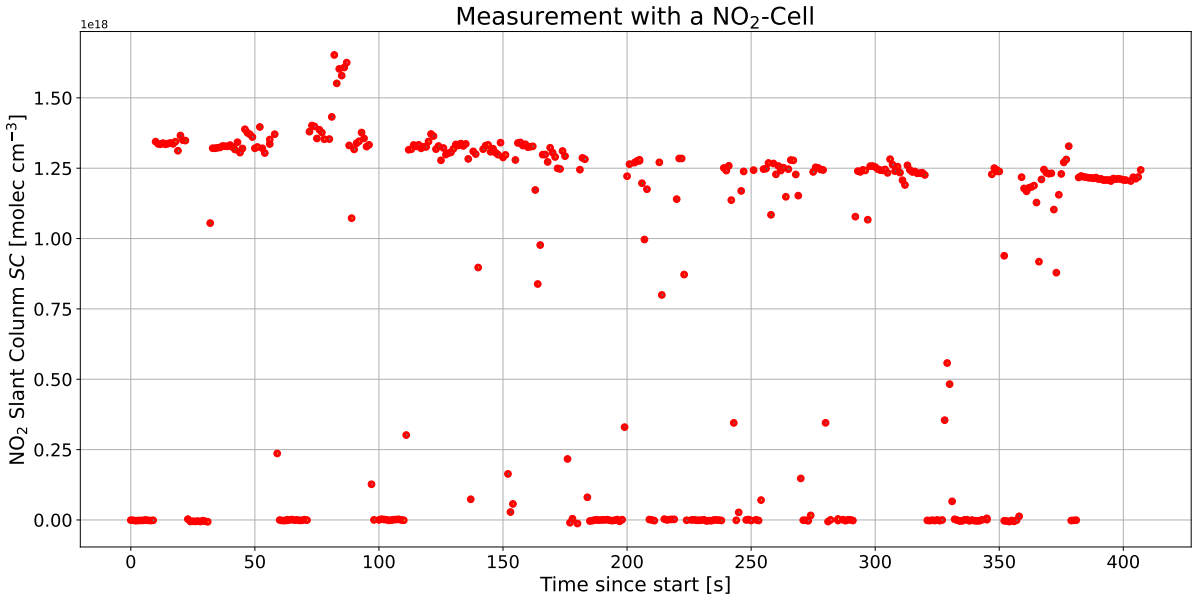


Figure 6.2: The measured NO_2 slant column SC for the measurements with the NO_2 cell.

cm^{-3} by the end of the measurements. Since multiple spectra are averaged into one, there are some measurements in which the NO_2 cell was only in the light path for a few individual measurements. This results in a lower measured NO_2 content. In combination with tilting the cell, this results in a variation of the measured NO_2 columns. For these measurements, values ranging between $0.80(3) \cdot 10^{18}$ molec cm^{-3} and $1.65(6) \cdot 10^{18}$ molec cm^{-3} were measured.
As the NO_2 content in the cell is quite high, the simplified DOAS-fit yields plausible results, that can be easily distinguished and observed in real time.

6.2 Long-term measurement

In order to assess the quality of the Avantes Nexos spectrometer, a long-term measurement using daylight was conducted. The measurement started at around 12:00 CEST and ended at 21:00 CEST and was conducted on a sunny day with minimal cloud coverage. As the reference for the DOAS fit, a previous measurement was used. Parallel to this, an Avantes AvaSpec spectrometer with the same viewing angle of around 30° and direction as the Nexos was taking measurements. Both spectrometers were facing west. Figure 6.3 shows the spectra measured with both spectrometers. For this measurement, the AvaSpec was calibrated using the Fraunhofer lines located in the wavelength range of the spectrum, which yields a good calibration in the wavelength region between 385 nm

and 460 nm. A comparison of the results is shown in Fig. 6.4.

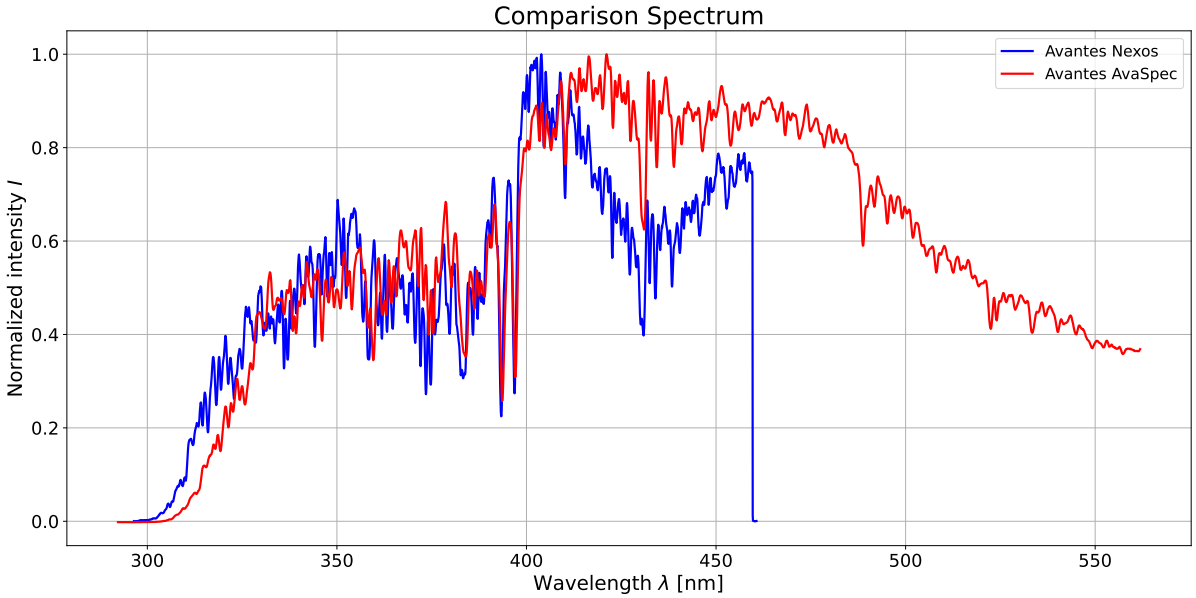


Figure 6.3: The normalized spectrum for the two spectrometer Avantes Nexos (blue) and Avantes AvaSpec (red).

The NO_2 slant column SC_{Nexos} measured with the Nexos has a local maximum of $5.7(3) \cdot 10^{15}$ molec cm^{-3} at noon. After noon, SC_{Nexos} decreases by $7.3(13) \cdot 10^{15}$ molec cm^{-3} and starts increasing again at 14:00. With the setting of the sun, and therefore a longer light path, SC_{Nexos} increases sharply and reached a value of $7.8(3) \cdot 10^{16}$ molec cm^{-3} at the end of the measurements.

The measurements taken with the AvaSpec had a lower exposure time than the Nexos and still reached saturation between 17:00 and 18:00 and between 18:30 and 20:30. This causes gaps in the measurements. The NO_2 slant columns SC_{AvaSpec} measured with AvaSpec has similar trend to the measurements with the Nexos. Between 15:00 and 18:30, SC_{AvaSpec} is consistently lower than SC_{Nexos} by about $0.9 \cdot 10^{15}$ molec cm^{-3}. After 20:30, the AvaSpec spectrometer instead measured a higher NO_2 slant column, with a maximal difference of $5.19(103) \cdot 10^{15}$ molec cm^{-3}.

Throughout the afternoon, the measured slant columns SC_{Nexos} and SC_{AvaSpec} fluctuates. However, these fluctuations are seen for both spectrometers and therefore, were caused by effects in the atmosphere. Generally, the spectrometers are in good agreement.

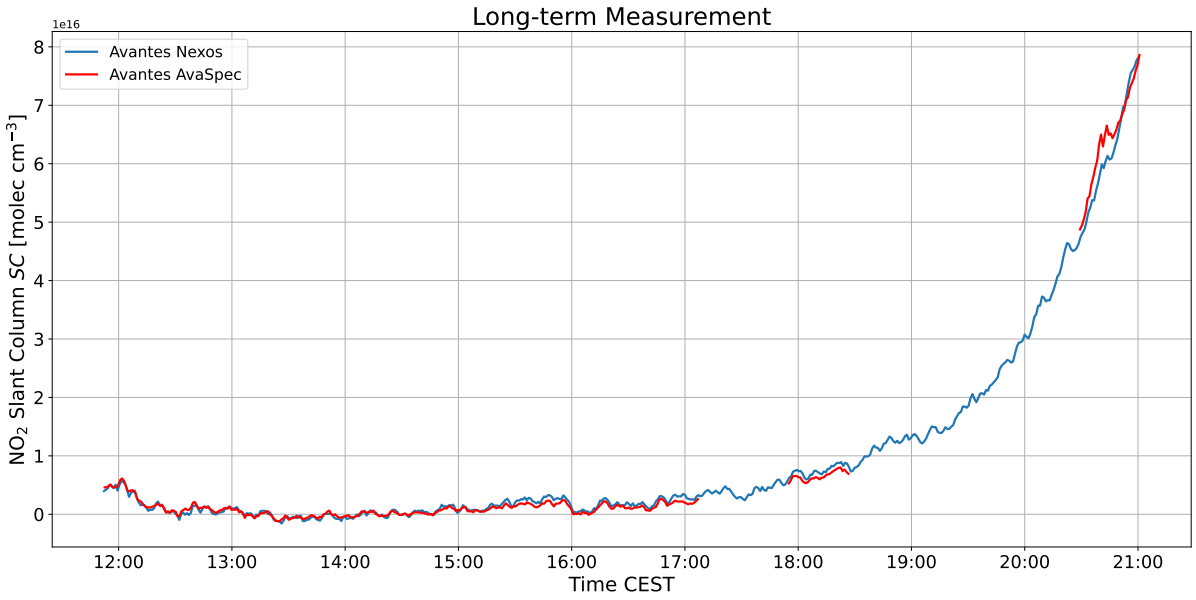


Figure 6.4: The measured NO_2 slant column SC for the long-term measurements using the Avantes Nexos and Avantes AvaSpec spectrometers.

7 Field measurements

Field measurements with the Drone-DOAS-System were conducted on the 13th of July and 3rd of August 2026. The target of the these measurements was the plume emitted by steel works "ArcelorMittal" in the harbour district of Bremen, which is shown in the picture in Fig. 7.1.



Figure 7.1: Picture of the steel works taken with the UAV on the 13th of July 2026.

The main chimney, which is referred to as the source, has a height of 125 m and is located at 53° 7′ 29.2” N and 8° 41′ 17.31” E. Other potential potential sources of NO_2 emissions in that region include the harbour power plant and the two smaller chimneys of the steel works with heights between 100 m and 110 m.
As shown in Fig. 7.2, the flights were conducted in the Niedervieland area in Bremen-Seehausen on the left side of the Weser river, in order to keep the distance from houses, power lines and major roads as required by law. Therefore, the distance D to the source was about 1.5 km for both flights.

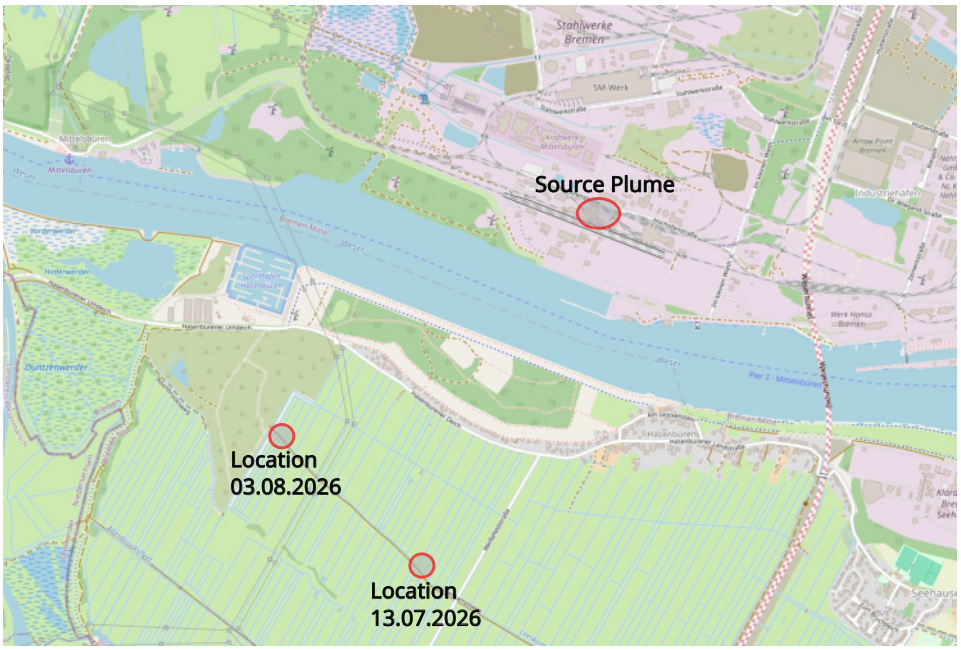


Figure 7.2: A map showing the Niedervieland area and parts of the harbour of Bremen, with the locations of the flights and main source of the plume marked.

Per day, two separate flights were performed, with a maximum flight height $h_{\mathrm{UAV,max}}$ of 120 m above ground level (a. g. l.), although during the first day, only a height of 100 m a. g. l. was reached.

7.1 Results of the flight on the 13th of July 2026

The first flights were conducted on the 13th of July 2026 and were used as test flights. Thus, not everything, like the positioning of the optical fibre, was final yet. Figure 7.3 shows the weather conditions during the first flights. The wind came mostly from the east with a maximum wind speed v of $10.3(3)\,\mathrm{m\,s^{-1}}$, measured at a height h_{UAV} of 52 m and an average wind speed v of $3.4(16)\,\mathrm{m\,s^{-1}}$ across all heights. The UAV was

assembled in the sunlight and therefore, the temperature T measured by the two sensors on the measurement platform reached a maximum of 40.0(3) °C on the ground. Before the second flight of the day, T had only a maximum of 33.4(3) °C. The temperature T decreases with altitude and reached a minimum of 25.5(3) °C at an altitude of 100 m

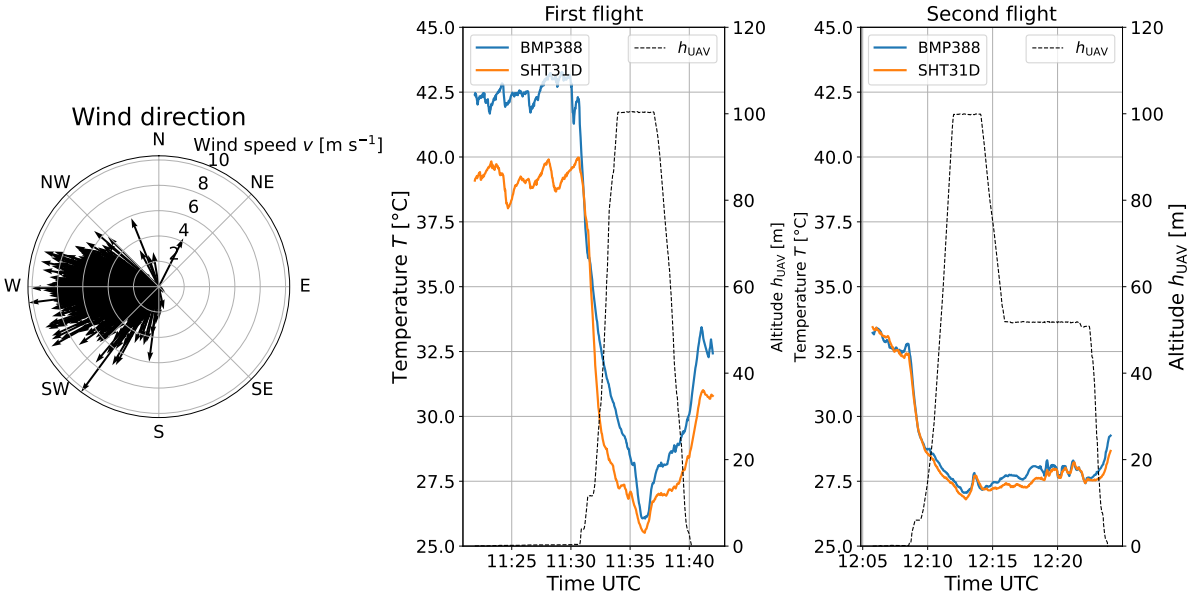


Figure 7.3: a) Wind direction and wind speed v measured on the 13th of July 2026 and b) the temperature T measured using the Bosch BMP388 (blue) and the Sensirion SHT31-DIS (orange) sensors during both flights with the altitude h_{UAV} at which it was measured.

During the first flight, the holder of the optical fibre was placed on the front half of the measurement platform next to the Raspberry Pi looking forward. Since the spacing block was not used by now and the viewing angle of the telescope had not been calibrated, the angle α of the optical fibre was estimated to be around 30° in order to keep clear of the rotors. At a distance D of approximately 1.5 km to the plume and the maximum height of the UAV $h_{\mathrm{UAV,max}}$ of 120 m a. g. l., the measured height h_{meas} of the plume for the first flight was between 866 m and 966 m. Taking the pitch angle α_{pitch} with a maximum of 4.7° into consideration, a height up to 1039 m was determined at the distance of the plume.

For the first flight, the flight pattern was a simple upwards movement until $h_{\mathrm{UAV,max}}$ was reached. At that height, yaw rotations were performed to find the NO_2 plume. As shown in Fig. 7.4, only low columns of NO_2 were observed, with SC usually reaching up to $2 \cdot 10^{16}$ molec cm^{-3} and a peak of $5.3(3) \cdot 10^{16}$ molec cm^{-3}, when the UAV was still

on the ground and tilted. For these measurements, the same reference spectrum as in Sect. 6.1 was used.

The first flight showed that the plume was lower than 866 m, since at higher altitudes

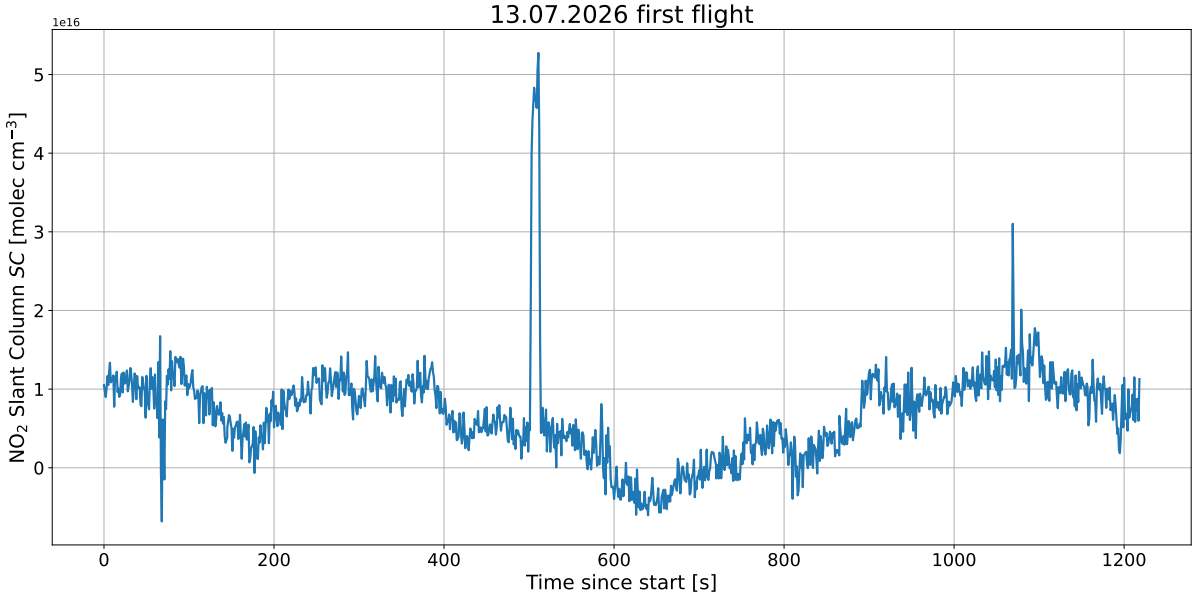


Figure 7.4: The measured NO_2 slant column *sc* over time for the first flight on the 13th July.

h_{meas} only an average of $0.7(6) \cdot 10^{16}$ molec cm^{-3} were measured. Thus, the viewing angle α of the optical fibre was changed for the second flight. At the current position of the optical fibre holder next to the Raspberry Pi, the viewing angle could not be lowered without damaging the rotor and the holder. Therefore, the optical fibre was placed on the back half of the measurement platform. In order to be able to properly secure the holder, it was placed diagonally on the platform with the telescope facing backwards with an angle of 166° relative to the front of the UAV, shown in Fig. 7.5.

For the second flight, the viewing angle α of the fibre was set to approximately 10°. The flight pattern for this flight was similar to the first flight, with the UAV moving upwards until $h_{\text{UAV,max}}$ and rotating to find the plume. While descending, the UAV was stopped at an altitude h_{UAV} of 50 m and moved forwards and backward to increase the pitch angle α_{pitch} to -14.2° and 17.7°, respectively. The second flight, therefore, covered a height h_{meas} up to 864 m at a distance D of 1.5 km. At these altitudes h_{meas}, higher columns of NO_2 were measured, see Fig. 7.6.

At single positions, columns above $8 \cdot 10^{16}$ molec cm^{-3} could be measured with a maximum of $9(5) \cdot 10^{16}$ molec cm^{-3}. Overall, at these heights an average of $3(2) \cdot 10^{16}$ molec cm^{-3}



Figure 7.5: Picture of the assembled UAV before the second flight on the 13th of July

were measured.

In order to calculate the spatial distribution of the measured signal, the plume is assumed to be located along the latitude ϕ_S of the source. This assumption is plausible since the wind mostly came from the east. For the spatial distribution, the distance Δ_{ij} and angle β_{ij} between two positions i and j are needed

$$\Delta_{ij} = \sqrt{\Delta\phi_{ij}^2 + \Delta\lambda_{ij}^2} \tag{7.1.1a}$$

$$\beta_{ij} = \arctan\left(\frac{\Delta\phi_{ij}}{\Delta\lambda_{ij}}\right) \tag{7.1.1b}$$

with $\Delta\phi_{ij}$ as the difference in latitude and $\Delta\lambda_{ij}$ the difference in longitude. Using (7.1.1), an azimuth angle θ can be calculated

$$\theta = \arccos\left[\frac{\Delta\phi_{S0}}{\sqrt{\left(\frac{\Delta\phi_{Si}}{\cos(\alpha_{yaw,i})}\right)^2 + \Delta_{0i}^2 - 2\left(\frac{\Delta\phi_{Si}}{\cos(\alpha_{yaw,i})}\right)\Delta_{0i}\cos(90 + \beta_{0i} - \alpha_{yaw,i})}}\right] \tag{7.1.2}$$

with the S being the location of the source and the 0 the start position at 53°06'44.2"N

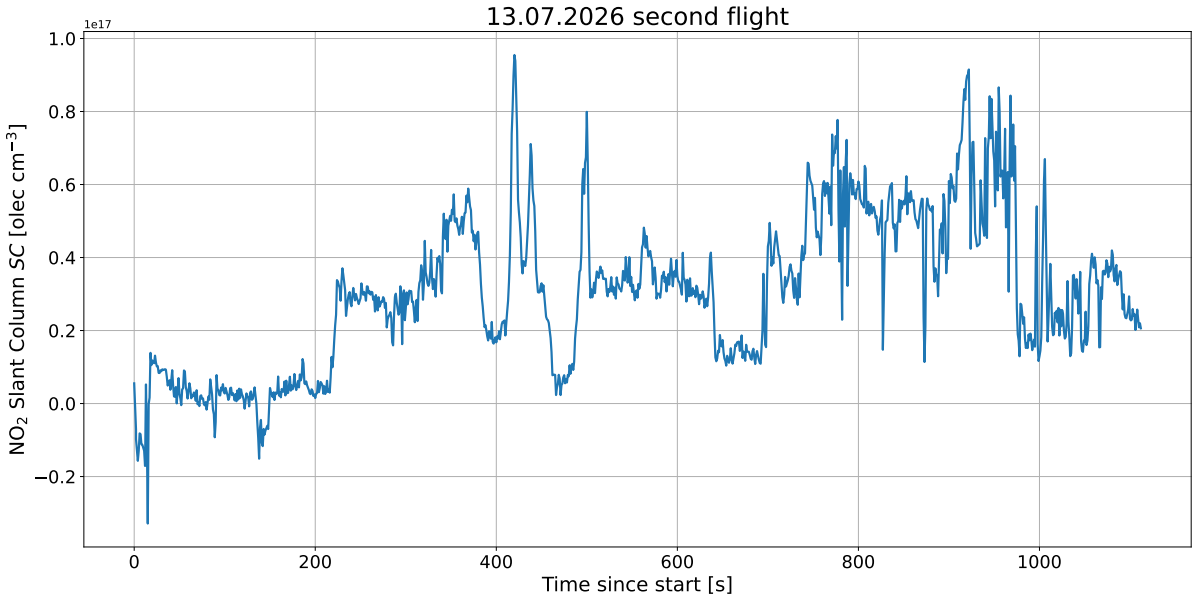


Figure 7.6: The measured NO_2 slant column SC over time for the second flight on the 13th of July.

and 8°40'33.3"E. The azimuth θ describes the angle between the orientation of the UAV and 0° north relative to the starting location.

Figure 7.7 shows the altitude h_{meas} of the measured NO_2 columns at different azimuth angles θ for both flights. It can be seen, that the high columns are located at an altitude h_{meas} between the ground and 600 m. Most of the plume is located between an azimuth θ of -50° and 10° with higher columns measured close to -10°. For greater absolute θ and altitudes h_{meas} above 600 m, the NO_2 generally decreases.

The dispersion of the plume depends on the atmospheric stability. Given the weather conditions on that day of high winds and moderate solar radiation, the plume would have a neutral stability. It would be expected that the plume spreads out more horizontally in the direction of the wind than vertically, although the spread in both directions is still quite similar (Krause 2023).

The results show that the plume spread out towards the west and upwards rather evenly, agreeing with the expectations.

Even though, weather and plume were not ideal, the test flight was very successful as a vertical and horizontal distribution of NO_2 was measured. The flight also provided insights on improvements to the measurement system.

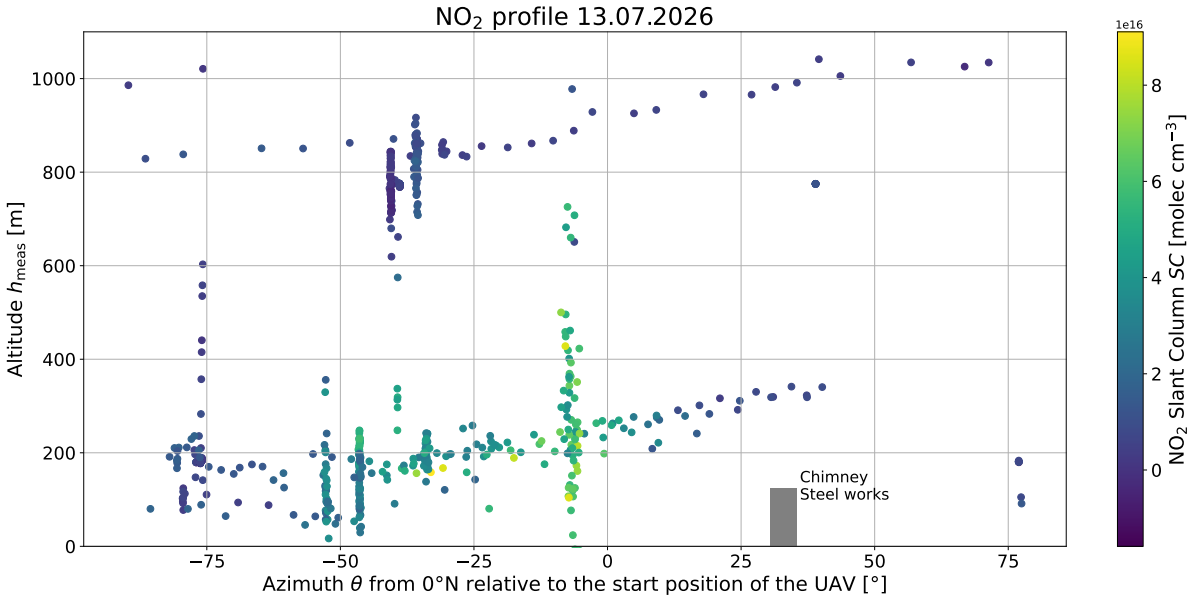


Figure 7.7: The measured NO_2 slant column SC at the height h_{meas} over the azimuth angle θ between the orientation of the UAV and 0° north relative to the starting location on the 13th of July.

7.2 Results of the flight on the 3rd of August 2026

A second pair of flights was conducted on the 3rd of August 2026. The weather conditions were similar, seen in Fig. 7.8, with winds coming from an eastern to a southeastern direction. While on the first day only a few gusts of strong winds occurred, the wind speed v averaged at $3.9(24)\,\mathrm{m\,s^{-1}}$ on the second day with the wind being noticeably stronger during the second flight, averaging at $5.4(19)\,\mathrm{m\,s^{-1}}$. The temperature T ranged from $38.7(3)\,°\mathrm{C}$ on ground level to $26.2(3)\,°\mathrm{C}$ at an altitude h_{UAV} of $120\,\mathrm{m\,a.g.l.}$.
Between the two measurement days, the system was improved. Besides some software updates regarding the data storage, the most important improvements were applied to the optical fibre. The usage of a 2 cm high spacing block underneath the fibre holder allows for the fibre to sit higher while facing forward, avoiding the rotors even at low angles. Additionally, the angle had been calibrated and during both flights, the viewing angle α was set to the marking of 10.649(2)°.

Especially during the second flight, strong winds drained the batteries of the UAV, cutting the flight time short to around 15 min. These amplified the difficulties in finding the plume and, due to the time limitations, no patterns were flown that day. As shown in Fig. 7.10, high columns of NO_2 were measured with values reaching $10.1(3)\cdot10^{16}\,\mathrm{molec\,cm^{-3}}$. However, these peaks could not be located again while measuring, since the UAV moved

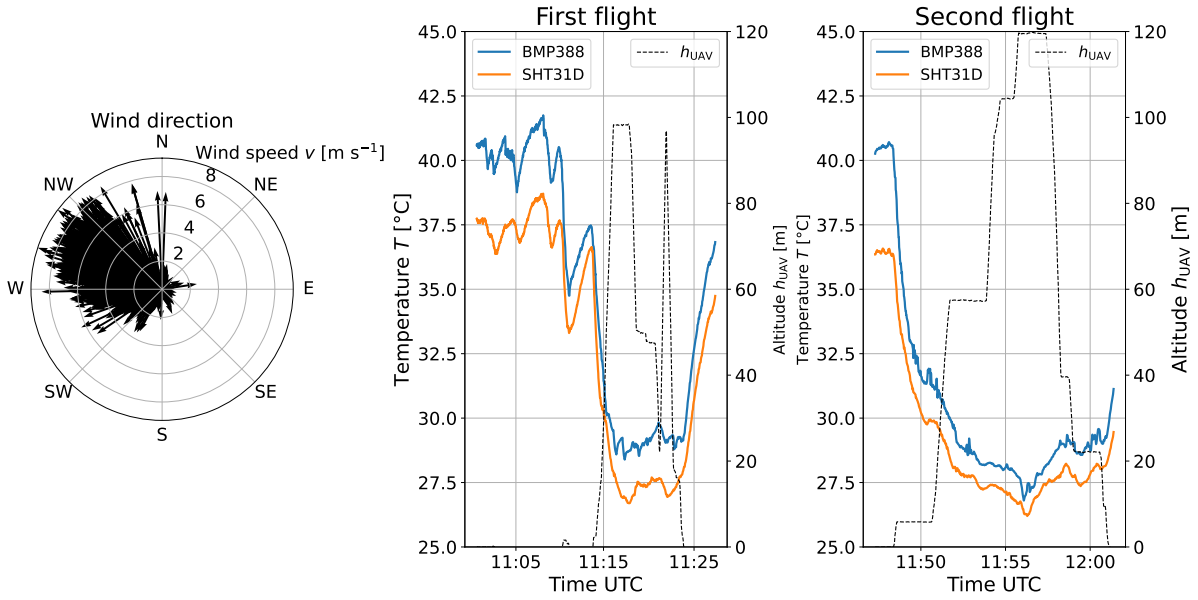


Figure 7.8: a) Wind direction and wind speed v measured on the 3rd of August 2026 and b) the temperature T using the Bosch BMP388 (blue) and the Sensirion SHT31-DIS (orange) sensors measured during both flights with the altitude h_{UAV} at which it was measured.



Figure 7.9: Picture of the UAV on the 3rd of August 2026.

faster than the time between two transmitted data packages, as well as due to it being unstable due to wind. Plotting the altitude h_{meas} and the relative azimuth θ of the mea-

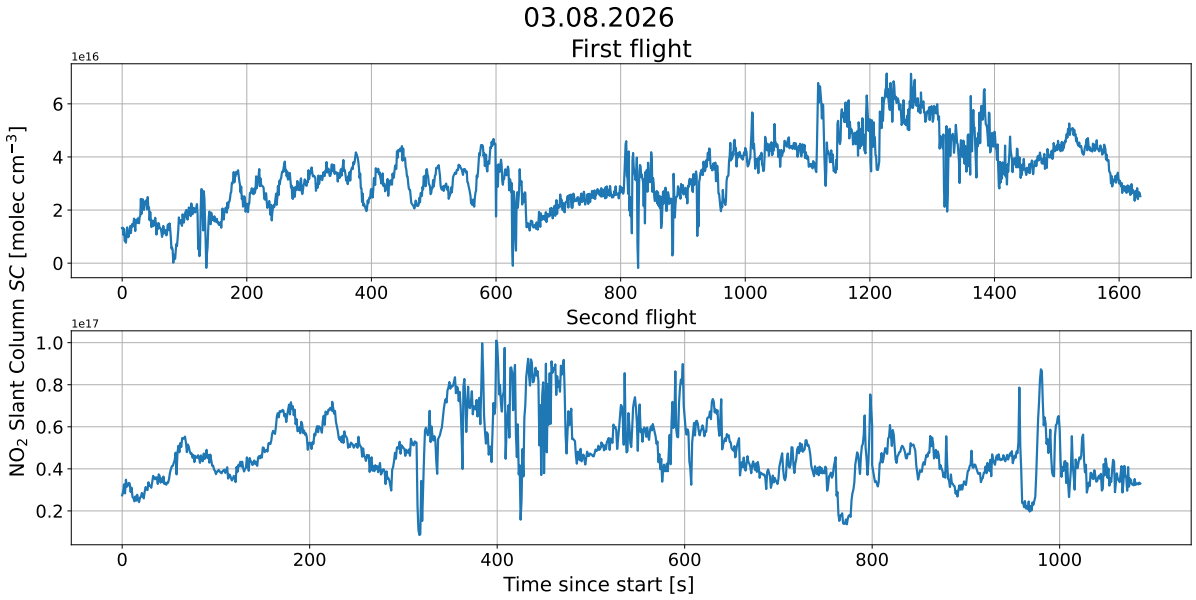


Figure 7.10: The measured NO_2 slant column SC over time for the both flights on the 3rd of August.

surement using (7.1.2), Fig. 7.11, it can be seen that a low altitude of the plume was found. The high columns of NO_2 were measured at an azimuth θ between -25° and 50° at

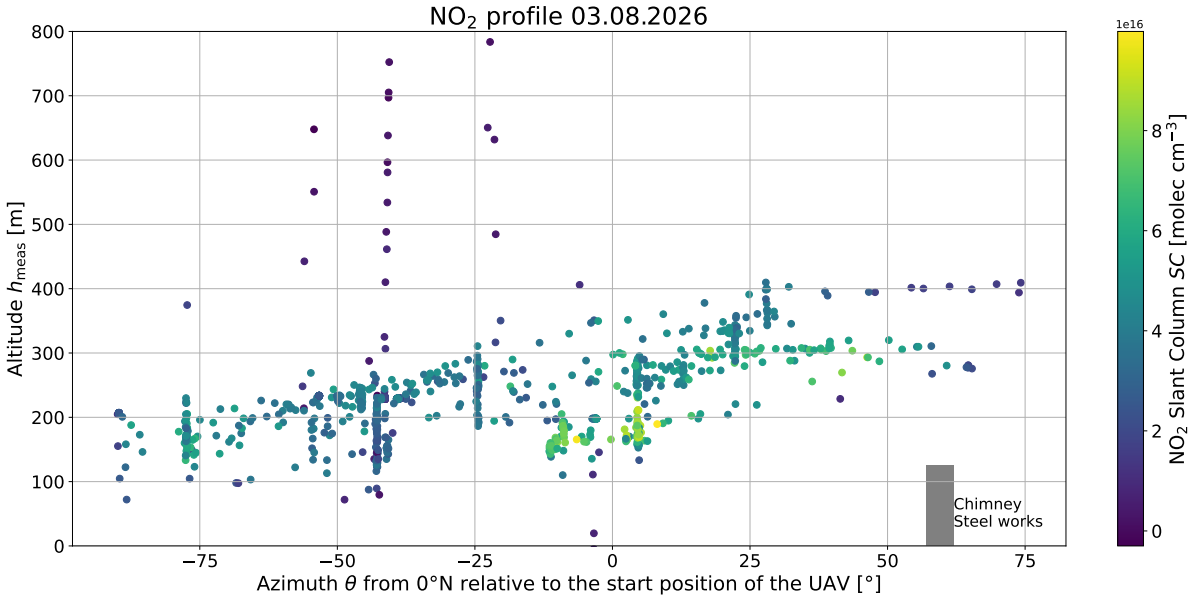


Figure 7.11: The measured NO_2 slant column SC at the height h_{meas} over the azimuth angle θ between the orientation of the UAV and 0° north relative to the starting location on the 3rd of August.

an altitude h_{meas} of 200 m. For altitudes above 400 m, the NO_2 column decreases, likewise

for an azimuth θ greater than -25°, with a few exceptions. Most of the plume measured lies between an azimuth θ of -10° and 50° with an average of $3.9(15) \cdot 10^{16}\,\mathrm{molec\,cm^{-3}}$ and an altitude h_{meas} below 300 m.
Since the weather conditions were similar to the 13^{th} of July, it would also be expected that the plume spread out almost evenly, horizontally and vertically. The measured plume spread mostly horizontally as expected. However, altitudes h_{meas} above 400 m were only sparsely measured.

While overall the measurement system, and especially the improvements since the first flight, worked and NO_2 was measured, problems during the measurement still occurred. These problems were mainly caused by the weather since, especially towards the end, the wind came more from the south east causing the plume to be in a location that cannot be measured from a position where the UAV is allowed to fly. Additionally, it was noticed that the frequency at which the measurements are saved and transmitted to the groundstation decreases over time. For these measurements the frequency was set to twice per second, which was never reached. By the end, the data packages were transmitted on average once every two seconds.

8 Improvements and outlook

During the field measurements, problems with the Drone-DOAS-system became apparent. While some problems could be solved within the scope of this thesis, some still remain.
During the flights, the weather was not ideal, which caused difficulties finding the plume. These were worsened by high winds, resulting in a reduction of flight time due to a higher power consumption. This leads to the problem that, due to the fixed angle of the optical fibre, many time and power consuming manoeuvres have to be flown in order to find the plume. Moreover, this was complicated by a delay between the taking of the measurement and the reception of a data package by the groundstation. Since the UAV can move significantly between the sending of two data packages, either due to the drone being controlled too quickly or due to the drone having troubles maintaining its position in high winds, it is possible that even if high NO_2 columns are measured, the exact direction cannot be determined with certainty. During the measurements, it was also noticed that the frequency at which the data packages were transmitted decreased over time. Since a data package is sent by the fly-script, this means that the frequency at which the data

is saved decreases, too. This leads to the major problem that the measurements can no longer be assigned to a precise location or orientation of the UAV. The search for the plume could potentially be simplified by having the possibility of changing the viewing angle of the optical fibre mid-flight. This would only work if a motor is used, which was omitted due to mass constrictions. However, this could be realised by creating a new measurement platform with only the most important measuring devices, to have more capacity available for the optical fibre. A motorized adjustment of the viewing angle has the advantage of knowing the exact angle during the flight. Furthermore, it allows for a scanning of the plume while the UAV is stationary. This would save time and power, making statements about the plume's position more quickly and easily, resulting in more time for the actual measurement.

The slowing down of the fly-script could have multiple causes. On one hand, an older Raspberry Pi with little RAM was used. Therefore, it is possible that the Raspberry Pi is overloaded during the measurements and slows down. This could be resolved by using another small computer with more RAM. However, it is more likely that the problem is caused by the software, more specifically the read-out of the recorded data, as the writing of the spectra by the spectrometer is not affected. Figure 8.1 shows the time Δt that the fly-script needs between the read-out of two measurements, for different numbers of measuring devices. It can be seen that the time Δt increases from a length of 1 s at the beginning of the measurement to a length over 10 s after 15 min, when all measuring devices are used. When single devices are not taking measurements, this increase slightly decreases to a time Δt of 7.5 s after 15 min. But most importantly, it shows that Δt remains constant, when the spectrometer is not measuring. Therefore, reading the last spectrum causes a significantly delay in the execution of the fly-script as the measuring time progresses. This problem can easily be solved by saving the last spectrum separately in a temporary file and having the fly-script interact with this file. As a result, the sampling time remains constant over the entire measurements. It should be noted that the measurements shown here represent an extreme case and during the test and field measurements, this increase was lower. This is the reason, why the problem was not identified and the solution was not implemented earlier. This performance could potentially be further improved by using a faster programming language than Python.

Additionally, the high amount of straylight in the wavelength range below 425 nm needs to be filtered, if gases other than NO_2 are to be measured. The current setup does not allow for a filter to be implemented and therefore, has to be adjusted.

Lastly, the spacing block is only 3D-printed, while it withstood a flight with high winds

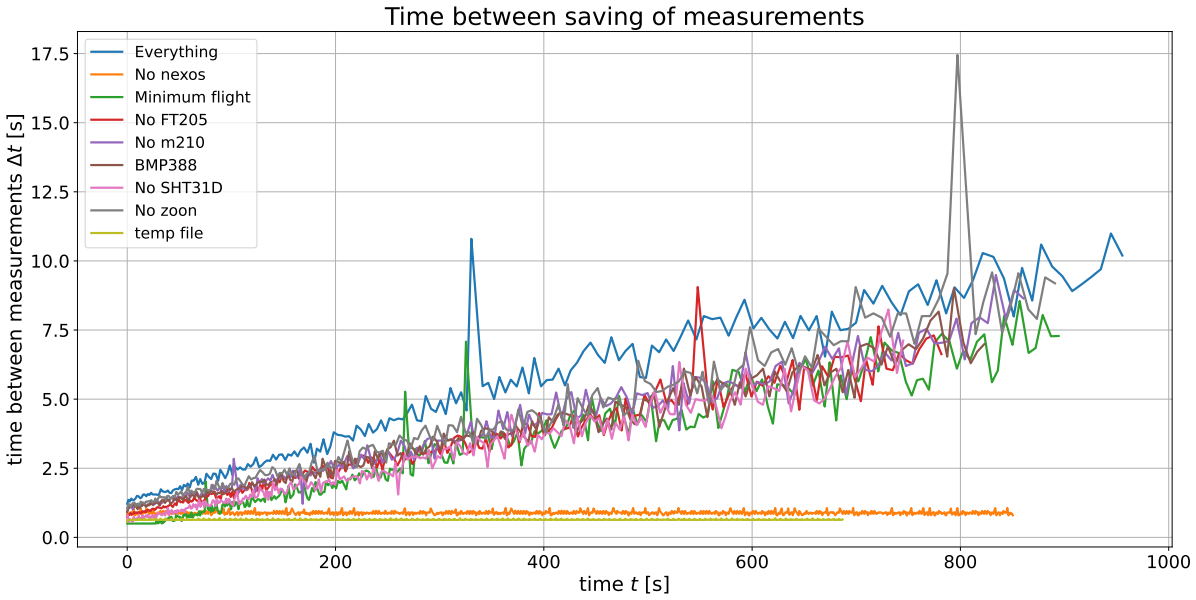


Figure 8.1: The time Δt between measurements done by fly-script over time t for different amount of measuring devices enabled.

without any visible damages, long-term durability is not given and a more solid solution needs to be considered.

In general, the system could be improved and expanded using a larger drone, which has the advantage of longer flight times and higher payload. A higher payload would allow to implement a motorized adjustment of the viewing angle as well as the opportunity to insulate the spectrometer to minimize temperature changes. With these improvements, measurements of a plume should become easier. Especially the possibility of scanning for the plume simplifies the search for it, leaving more time for the actual measurements. Nevertheless, a functioning measuring system for drone-based DOAS measurements was created. The system can be used for further measurements of emissions plumes of other industrial sites. Furthermore, while it is also possible to measure emissions from shipping and road traffic, the distances required by law must be adhered to, potentially complicating the measurements.

9 Conclusion

In this thesis, a measuring system to conduct drone-based DOAS measurements was created. The system is a modification of the CO_2 measuring CRUSOE-System by Reuter et al, using the same DJI Matrice 210v2 UAV. The CO_2 sensor, mounted to a bayonet connector on the underside of the UAV, was replaced by compact Avantes Nexos spectrometer, in order to measure NO_2. The optical fibre was laid close to the drone body to the top and placed in a specifically made holder, consisting of a foot and pole. The holder is mounted to a pre-existing measurement platform and its angle can be freely adjusted between flights. In total, the Drone-DOAS-system has a mass of 5768(7) g and a estimated flight time of 24.73 min under perfect weather conditions.
A Raspberry Pi 3B+ controls the measurements during a flight. This is done via three scripts, the watchdog-script that automatically starts the measurements during boot and constantly checks if they are still running, the AvaMeas-script that takes and saves the measurements of the spectrometer and the fly-script. The last one takes the measurements of the additional sensors mounted to the measurement platform and performs a simplified DOAS-fit to the last spectrum measured. While in the air, the most important data is transmitted to the groundstation running on a different PC as backup.
Characterization measurements performed confirmed the linearity of the detector for both the dark signal and measurements with a light source. The spectrometer was also wavelength calibrated using a HgCd spectral lamp with a polynomial relationship between the measured pixel PX and the wavelength λ of the peak. The measured peaks had a FWHM between 0.46 nm and 0.58 nm. Thus, the spectrometer has a usable wavelength range of 296 nm to 460 nm, which is not ideal for the measurement of NO_2, but offers the possibility to measure SO_2 in the future. During a flight, the ambient temperature T_{amb} can change significantly and the temperature of the spectrometer is not regulated. The measurements are, therefore, dependant on the temperature and can shift at an rate Δ_λ of $0.014(2)\,\mathrm{nm\,K^{-1}}$.
The influence of the polarization state and potential straylight was also tested. While the influence of the polarization state is negligible, straylight significantly impacts the measurements for wavelengths shorter than 425 nm.
The usage and well-adjusting of a telescope lens improved the numerical aperture NA of the optical system from 0.33(3) to 0.0169(17), resulting in the system having an acceptance angle θ of just $0.9666(17)\,^\circ$. Besides the telescope lens, the viewing angle of the optical fibre was calibrated as well, since, due to weight restrictions, the viewing an-

gle can only be adjusted manually on the ground. Four angles of 5.575(2)°, 10.649(2)°, 16.264(3)°, and 28.736(4)° were measured beforehand and marked on the foot of the optical fibre holder for easy adjustment.
Furthermore, the hardware and software of the measurement system was tested. The Avantes Nexos spectrometer was compared to an Avantes AvaSpec spectrometer and showed good agreement. The software of the Drone-DOAS-system works as intended, with the simplified DOAS-fit yielding plausible results.
Within the scope of this thesis, two flights in the field were conducted on the 13$^{\text{th}}$ of July and on the 3$^{\text{rd}}$ of August 2026. The flights were done in the Niedervieland area of Bremen and measured the plume emitted of the steel works on the right side of the Weser river. During both flights, the weather was not ideal with winds mostly from east and an unstable plume, making the measurements more difficult. Nevertheless, higher NO_2 columns of up to $10.1(3) \cdot 10^{16}\,\text{molec}\,\text{cm}^{-3}$ could be measured at an altitude of 300 m on the 13$^{\text{th}}$ of July and at an altitude of 200 m on the 3$^{\text{rd}}$ of August.
While the developed Drone-DOAS-system could still be improved, a working measurement system was created, that can be used as is to complement other DOAS measurements.

References

Abougarair, Ahmed J., H. Almgallesh, and Nasar Aldian A. Shashoa (2024). "Dynamics and Optimal Control of Quadcopter". In: DOI: 10.1109/MI-STA61267.2024.10599742.

Baidar, S. et al. (2013). "The CU Airborne MAX-DOAS instrument: vertical profiling of aerosol extinction and trace gases". In: *Atmospheric Measurement Techniques* 6. DOI: 10.5194/amt-6-719-2013.

Berg, N. et al. (2012). "Ship emissions of SO_2 and NO_2: DOAS measurements from airborne platforms". In: *Atmospheric Measurement Techniques* 5. DOI: 10.5194/amt-5-1085-2012.

Demtröder, Wolfgang (2013). *Experimentalphysik 2*. 6. Aufl. Springer Spektrum. ISBN: 978-3-642-29943-8.

Dix, B. et al. (2009). "Airborne multi-axis DOAS measurements of atmospheric trace gases on CARIBIC long-distance flights". In: *Atmospheric Measurement Techniques* 2. DOI: 10.5194/amt-2-639-2009.

Fernando, Chandula and Matthew Adams (2025). "Capturing the vertical distribution of near-highway nitrogen dioxide using UAV-based measurements". In: *Geomatica* 77.1. DOI: https://doi.org/10.1016/j.geomat.2024.100043.

Foken, Thomas (2021). *Springer Handbook of Atmospheric Measurements*. Springer. ISBN: 978-3-030-52170-7.

Friedrich, M. M. et al. (2019). "NO2 vertical profiles and column densities from MAX-DOAS measurements in Mexico City". In: *Atmospheric Measurement Techniques* 12. DOI: 10.5194/amt-12-2545-2019.

General, S. et al. (2014). "The Heidelberg Airborne Imaging DOAS Instrument (HAIDI) – a novel imaging DOAS device for 2-D and 3-D imaging of trace gases and aerosols". In: *Atmospheric Measurement Techniques* 7. DOI: 10.5194/amt-7-3459-2014.

Hoffmann, Gabriel et al. (2007). "Quadrotor Helicopter Flight Dynamics and Control: Theory and Experiment". In: *AIAA Guidance, Navigation and Control Conference and Exhibit*. DOI: 10.2514/6.2007-6461.

Horner, R. P. et al. (2024). "Vertical profiles of global tropospheric nitrogen dioxide (NO_2) obtained by cloud slicing the TROPOspheric Monitoring Instrument (TROPOMI)". In: *Atmospheric Chemistry and Physics* 24. DOI: 10.5194/acp-24-13047-2024.

Kartal, Mehmet Akif (Mar. 2026). "Comprehensive aerodynamic and energy analysis of quadcopter propellers: an integrated CFD-experimental approach across RPM spectrum". In: *Engineering Computations*. DOI: 10.1108/EC-03-2025-0266.

Krause, Kai (2023). "Measurements of ship emissions using in-situ and LP-DOAS instruments". PHD thesis.

Lee, Suhyeon, Hyemin Hwang, and Jae Young Lee (2022). "Vertical measurements of roadside air pollutants using a drone". In: *Atmospheric Pollution Research* 13.

Liu, Emma J. et al. (2019). "Dynamics of Outgassing and Plume Transport Revealed by Proximal Unmanned Aerial System (UAS) Measurements at Volcán Villarrica, Chile". In: *Geochemistry, Geophysics, Geosystems* 20. DOI: https://doi.org/10.1029/2018GC007692.

Löffler-Mang, Martin (2012). *Optische Sensorik*. 1. Aufl. Vieweg+Teubner Verlag. ISBN: 978-3-8348-1449-4.

Meschede, Dieter (2008). *Optik, Licht und Laser*. 3. Aufl. Vieweg+Teubner. ISBN: 978-3-8351-0143-2.

Mueller, Mark W. (2025). *Dynamics and Control of Autonomous Flight*. 1st. Springer. ISBN: 978-3-031-91870-4.

Platt, Ulrich (2026). *Differential Optical Absorption Spectroscopy*. 2nd. Springer. ISBN: 978-3-662-68637-9.

Prados-Roman, C. et al. (2011). "Airborne DOAS limb measurements of tropospheric trace gas profiles: case studies on the profile retrieval of O_4 and BrO". In: *Atmospheric Measurement Techniques* 4. DOI: 10.5194/amt-4-1241-2011.

Raponi, Marcelo et al. (2018). "Development of a Volcanic Remote Monitoring System Based on the DOAS Technique". In: DOI: 10.1109/ARGENCON.2018.8646317.

Reuter, M. et al. (2021). "Development of a small unmanned aircraft system to derive CO2 emissions of anthropogenic point sources". In: *Atmospheric Measurement Techniques* 14. DOI: 10.5194/amt-14-153-2021.

Roedel, Walter (2024). *Physik unserer Umwelt: Die Atmosphäre*. 6. Aufl. Springer Spektrum. ISBN: 978-3-662-68943-1.

Rüdiger, J. et al. (2018). "Implementation of electrochemical, optical and denuder-based sensors and sampling techniques on UAV for volcanic gas measurements: examples from Masaya, Turrialba and Stromboli volcanoes". In: *Atmospheric Measurement Techniques* 11.

Schönhardt, A. et al. (2015). "A wide field-of-view imaging DOAS instrument for two-dimensional trace gas mapping from aircraft". In: *Atmospheric Measurement Techniques* 8. DOI: 10.5194/amt-8-5113-2015.

Stix, John et al. (2018). "Using Drones and Miniaturized Instrumentation to Study Degassing at Turrialba and Masaya Volcanoes, Central America". In: *Journal of Geophysical Research: Solid Earth* 123. DOI: https://doi.org/10.1029/2018JB015655.

Tian, Zhen-Yu (2025). *Environmental Chemistry: Advanced Concepts and Applications*. 1st. Springer. ISBN: 978-981-96-0072-4.

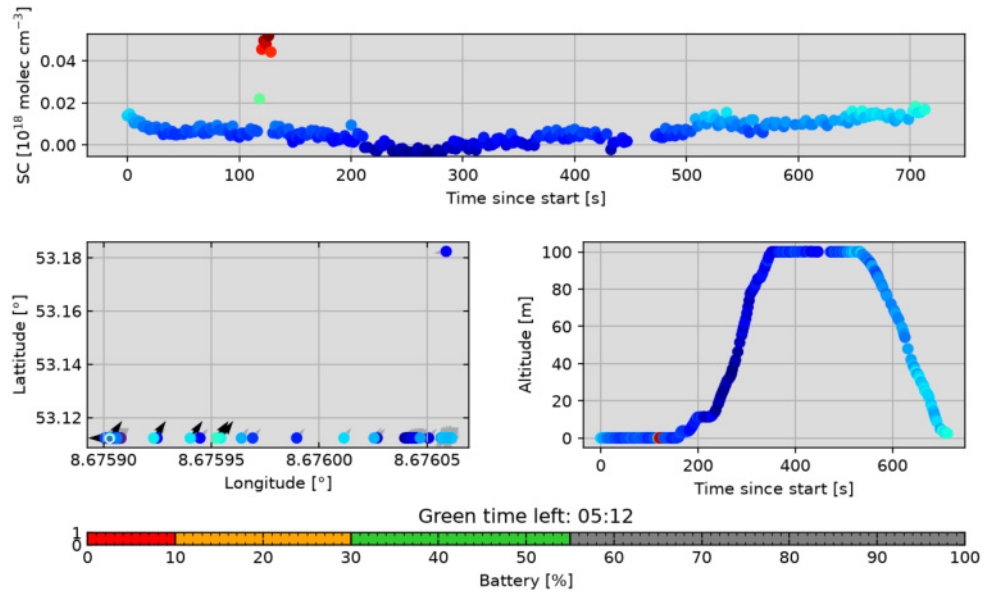
Vandaele, A.C. et al. (1998). "Measurements of the NO2 absorption cross-section from 42 000 cm1 to 10 000 cm1 (238–1000 nm) at 220 K and 294 K". In: *Journal of Quantitative Spectroscopy and Radiative Transfer* 59. DOI: https://doi.org/10.1016/S0022-4073(97)00168-4.

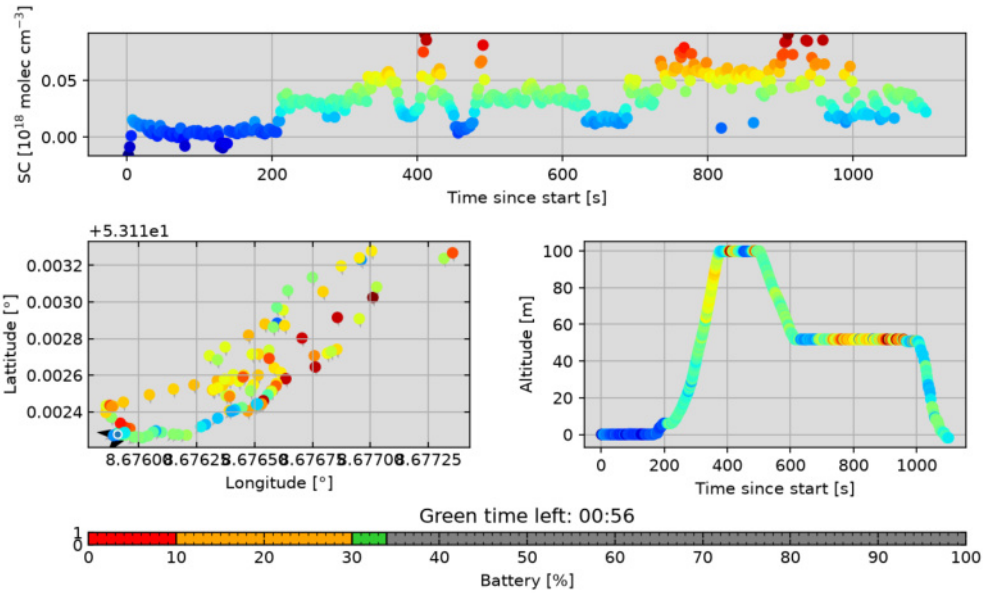
Vollmer, Michael (2025). *Optics*. 1st. Springer. ISBN: 978-3-031-99549-1.

Womack, C. C. et al. (2022). "A lightweight broadband cavity-enhanced spectrometer for NO_2 measurement on uncrewed aerial vehicles". In: *Atmospheric Measurement Techniques* 15. DOI: 10.5194/amt-15-6643-2022. URL: https://amt.copernicus.org/articles/15/6643/2022/.

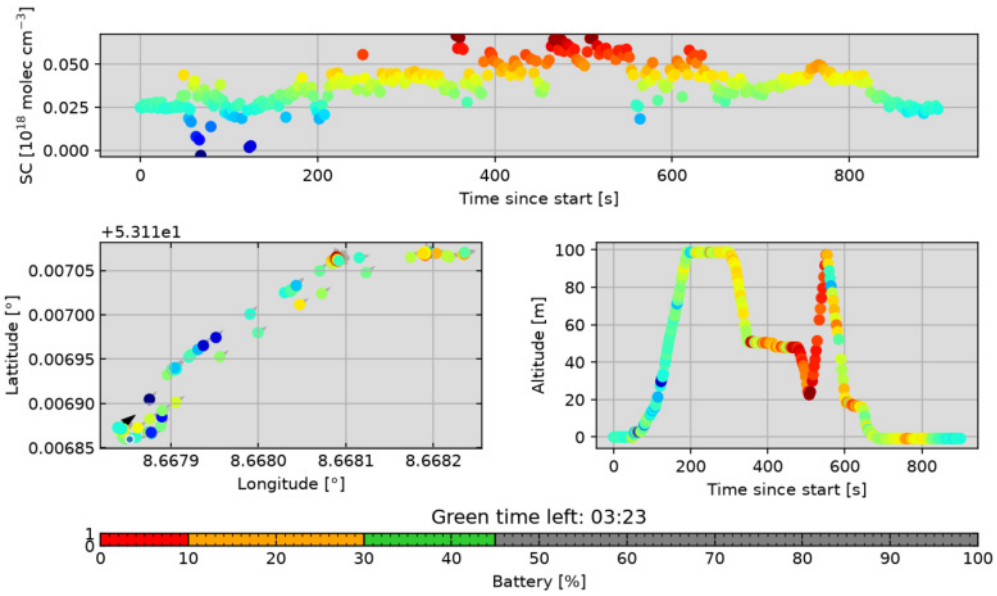
Appendix I: Groundstation plots

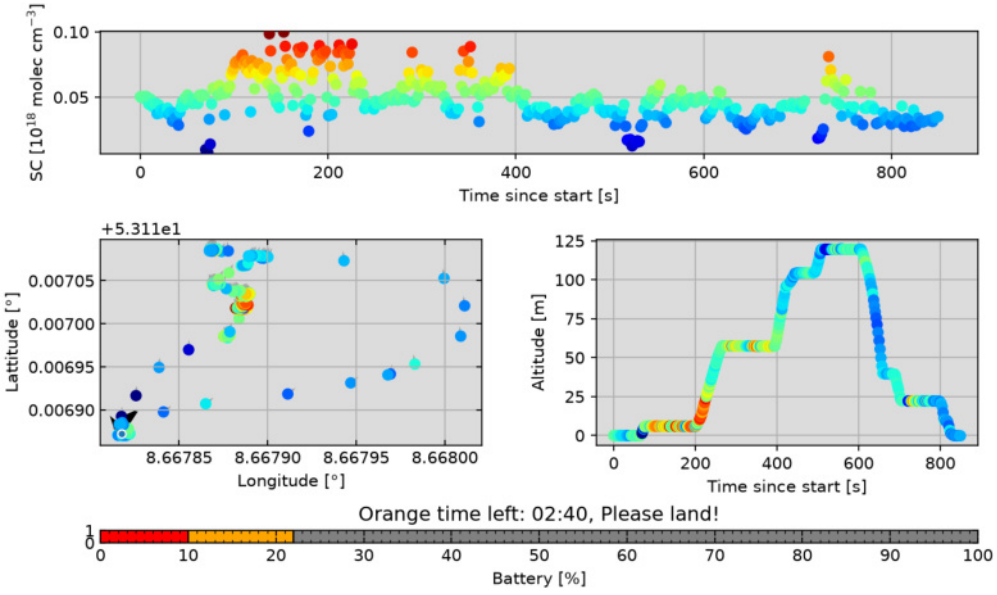
13.07.2026





03.08.2026





Appendix II: Instructions

Drone-DOAS

Step by step instructions for assembly and disassembly

This instructions manual explains step by step how to assemble the hardware of the Drone-DOAS measurement system

For disassembly, follow the steps in reverse order

Disclaimer: This manual does not replace the drone manufacturer's instructions for use, which must always be followed.

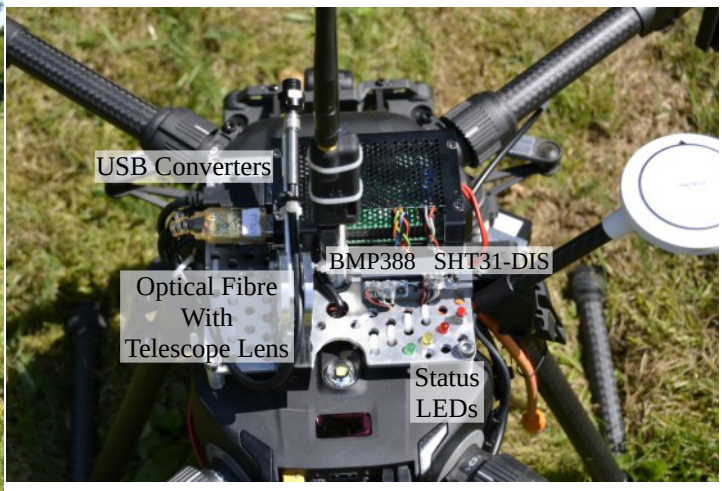


Extra Tools needed:

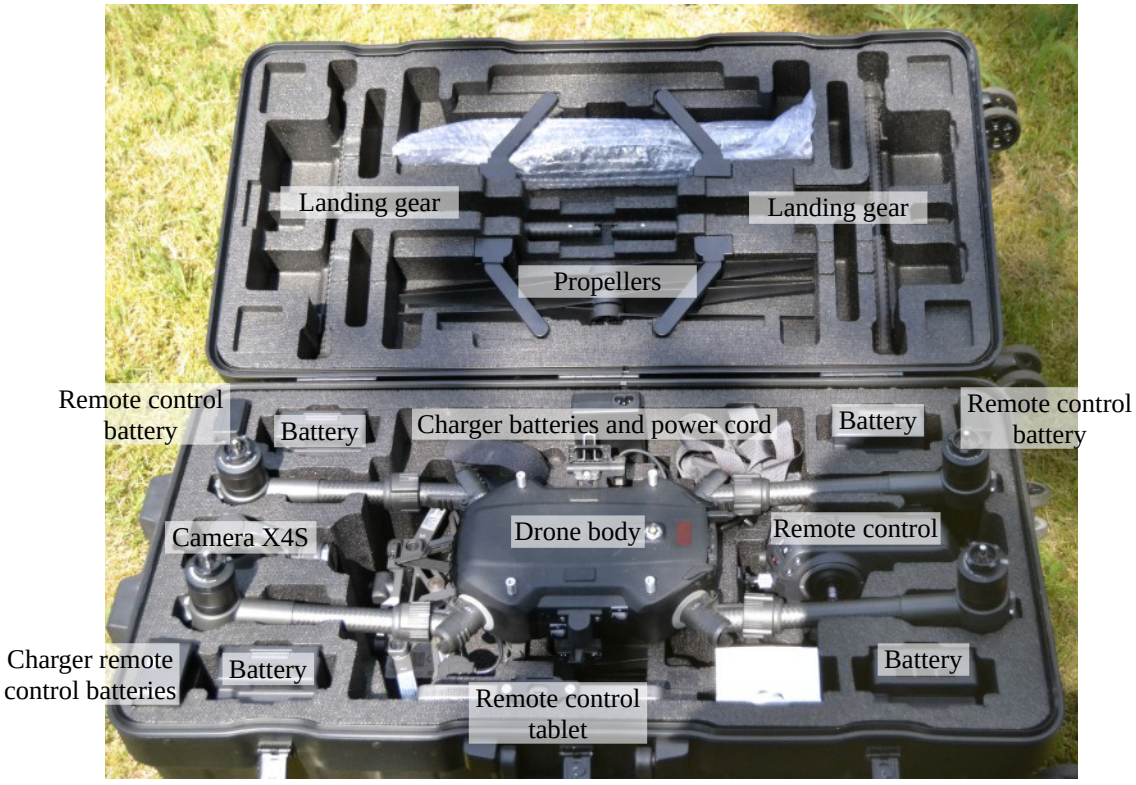
- Scissors and pliers
- Hex keys sizes 2.5mm & 4mm
- Zip ties
- Flathead screwdriver size 0.5mm

The assembled Drone-DOAS system





Contents of the drone rolling case



Landing gear and protective caps of the payload ports

Place the drone upside down

Tilt the GPS antenna away from the drone body

Insert and **lock** the landing gear (b)





Remove the protective caps of the payload ports

Press the release button on the side of the port (c)
Twist the cap

Make sure the connectors are **correctly aligned** (d)





Place the drone on the landing gear

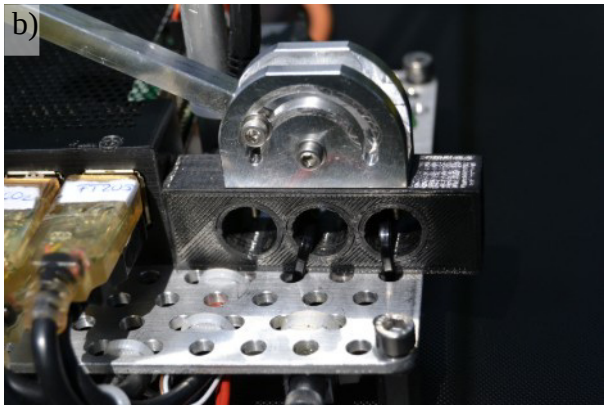
The measurement platform

a)



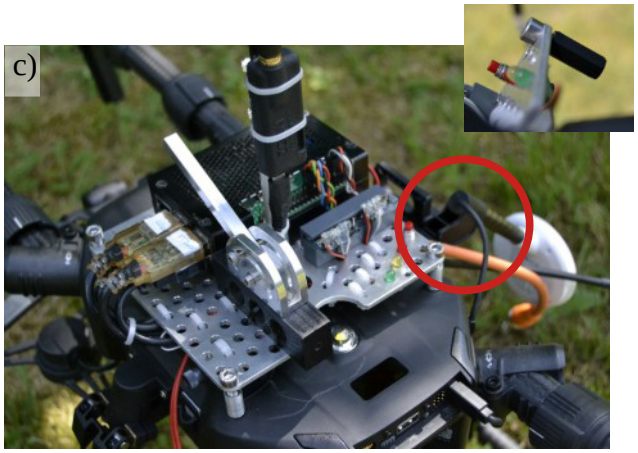
Mount the fibre holder onto the spacing block (a)
(This could also be done while the spacer is mounted to the platform)

b)



Secure the spacing block to the platform with zip ties (b)

c)



Remove the black nuts

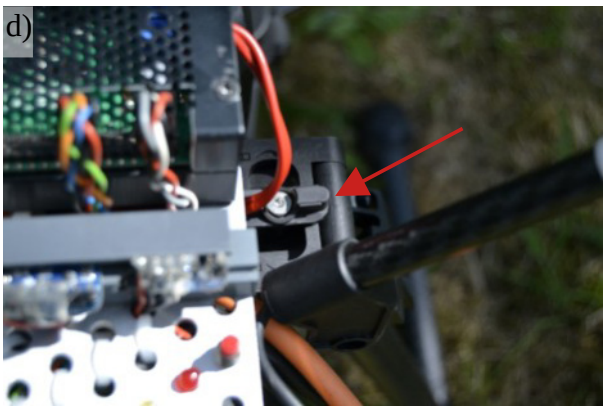
Place the platform on the drone (c)

The cut out is **above** the beaker light

The orange and black cable have to be **below** the cable of the GPS antenna

Tighten the screws

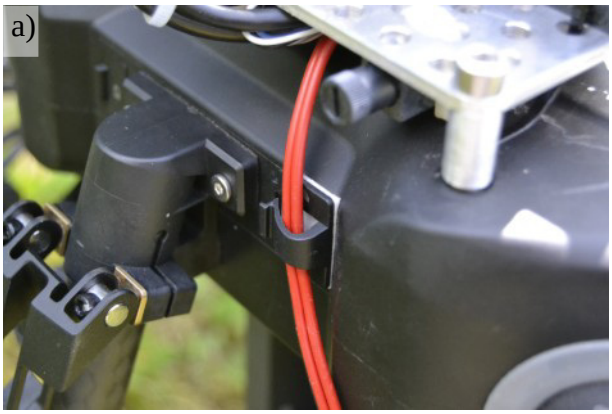
d)



Position the GPS antenna and **lock it** (d)

Wire laying and connecting cables

a)



Secure the cables of the measurement platform with the brackets on the side of the drone (a, b)

The orange cable is not used. To further **secure it**, tie it to the landing gear with a zip tie (b)

b)



Run the other cables underneath the arms of the drone

Connect the yellow power plug with the power port of the drone (c)

c)



Connect the black data cable to the OSDK port of the drone

Use the pins **directly next** to the connector of the GPS antenna (d)

d)



The spectrometer and optical fibre laying

a)

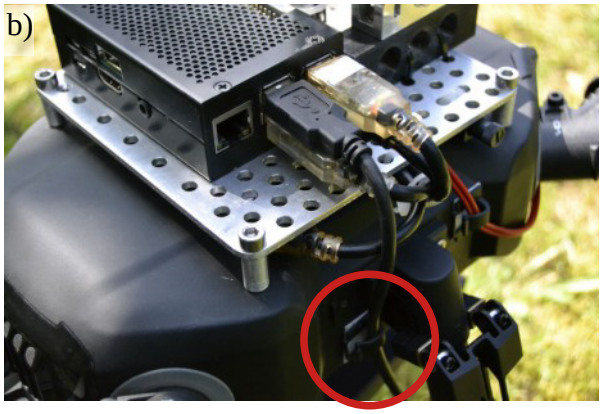


Twist the spectrometer in the bayonet connector of payload port 2 (a)

If used, twist the camera X4S in the bayonet connector of payload port 1

When it locks, it should click

b)



Unplug the top left USB converter labeled „CO2“

Tuck it **underneath** the measurement platform

Secure the spectrometer cable in the bracket

Plug in the spectrometer cable (b)

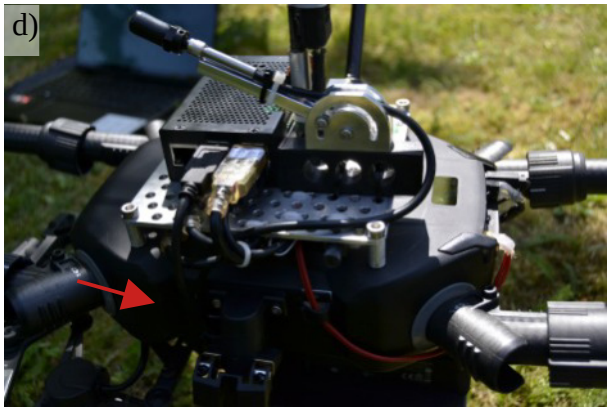
c)



Secure the optical fibre in the bracket on the underside of the drone (c)

Run the fibre past the battery compartment

d)



Secure it to one of the brackets on the side

Lay the fibre **underneath** the USB converters

Tie the end of the optical fibre to the fibre holder on the platform with a zip tie (d)

If needed, **further secure it** to the platform with a zip tie

Make sure the fibre is <u>not</u> in the way of the propellers

Drone arms and propellers

Bring the arms in flight position

Lock them in place by tightening the cap nut (a)

a)



Match the propellers to the correct arms
Grey to grey and black to black (b)

b)





Lock them by pressing down and twisting them

Make sure they are **properly locked** and
the metal in the middle **does not stand out** (c)

c)



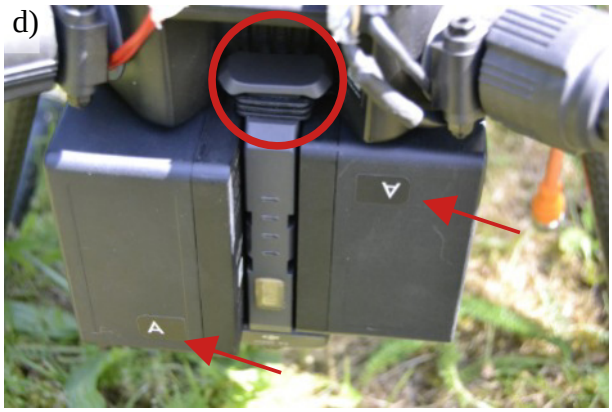
Flight batteries

Push the batteries firmly until they **snap into place**

Use only batteries **marked with the same letter** together

To release them, press the button (d)

d)



Protection

Remove the protective cover from the
wind sensor and telescope lens (e)

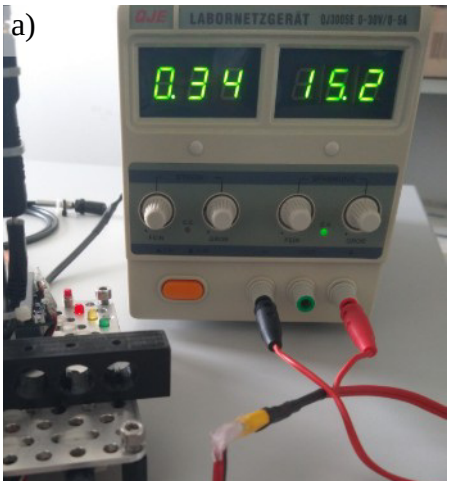
e)





External power supply (optional)

a)

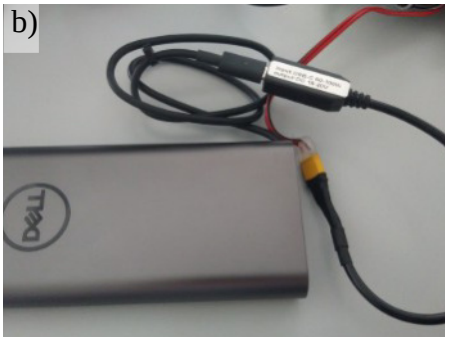


The measurement platform is powered by the batteries of the drone during the flight

Optionally, the measurement platform can also be powered externally

Use either a lab power supply (a)

b)



Or use a USB-C power bank with a USB-C to 18-20V step-up converter (b)

Monitor and LAN (optional)

c)



Optionally, the Raspberry Pi can be connected to a Monitor via the HDMI port and a LAN cable (c)

If a LAN cable is connected **during the boot**, the Pi assumes to be in the Lab and <u>does not start measuring</u>

Otherwise, the measurements will start automatically

If a monitor is connected, the current measurements are shown

Quick Guide to the Drone-DOAS Raspberry Pi

This is a quick guide to the basic operation of the Raspberry Pi on the UAV.

The Different Modes

The Raspberry Pi can start in two modes the „*Field Mode*“ and the „*Lab Mode*“. If nothing is connected to the Raspberry Pi, it assumes to be in the field and starts all measuring programms automatically. If the Raspberry Pi is connected to another PC via LAN cable or to the internet, it assumes to be in the lab and all measuring programms have to be started manually.
To make sure that the Raspberry Pi starts in the „*Lab Mode*“, have the LAN cable already connected during the boot. When the cable is disconnected, the Raspberry Pi switches to the „*Field mode*“ and starts the measuring programms. *This does not happen the other way around*, if the Raspberry Pi has started in the „*Field Mode*“ and switches to the „*Lab Mode*“, the measurements continue having the Pi effectivly still in the „*Field Mode*“.

Connecting to the Raspberry Pi

If a LAN cable is connected, connect to the Raspberry Pi with „*ssh pi@192.168.137.80*“, password:raspi123
To move files between PCs use:
scp raspi@192.168.137.80:Directory\FileNameOnPi Directory\FileNameOnPC (From Pi to PC)
scp Directory\FileNameOnPC raspi@192.168.137.80:Directory\FileNameOnPi (From PC to Pi)
To change the date of the Raspberry Pi:
sudo date -s „mon day year hh:mm“ (If watchdog was started before the date change, the file will have the old date in its name. If the measuring script is running during the time change, it will time out and restart.)

Where is What

Most frequently used files and folders can be found in the home directory „*home/pi/*“.
Measurements are save in the folder „*Measurements/*“.
DOAS specific scripts are in the folder „*Drohnen-DOAS/*“

Starting Scripts Manually

To make sure all dependencies are met and the scripts start correctly, start python within the virtual environment *env* using:
env/bin/python3 watchdog.py
env/bin/python3 fly.py
sudo env/bin/python3 Drohnen-DOAS/AvaMeas.py

The watchdog-script automatically starts the other two scripts in seperate tmux sessions. In order to attach to a session, use „tmux a -t fly“ or „tmux a -t meas“.
If the watchdog-script is terminated, e.g. via *„env/bin/python3 Shutdown_watchdog.py“*, *the measuring scripts will also be terminated*.

If a calibration or zenith measurement are to be performed, the Raspberry Pi has to be in the *„Lab Mode“* as only one script at a time can access the spectrometer.

Calibration and DOASconfig

A calibration of the spectrometer can be performed using „*sudo env/bin/python3 Drohnen-DOAS/AvaCal.py*“. The scripts takes a HgCd measurement with a corresponding dark measurement and saves them in the folder „*Measurements/Calibration/*“. When executed, the script „*DOASconfig.py*“ performs a wavelength calibration of the most recent line measurement and saves the result in the file „*DOASconfig.json*“.

Taking Dark and Zenith Measurements in the field

To take a dark and zenith measurement before the flight, execute the script „*AvaRef.py*“ with „*sudo env/bin/python3 Drohnen-DOAS/AvaRef.py*“ and follow the instructions. The measurements are saved in the folder „*Measurements/Reference/*“.
The most recent measurements will automatically be used by the measuring scripts.

To change the Exposure Time and other parameters, use „*sudo nano Drohnen-DOAS/Parameters.json*“. The changes will be used by *AvaMeas.py* and *AvaRef.py.*

Universität Bremen

Eigenständigkeits- und Einverständniserklärung zur Überprüfung mit Plagiatssoftware sowie die Erklärung zur Veröffentlichung bei Bachelor- und Masterarbeiten

Declarations of Authorship and Consent for Checking with Plagiarism Software and the Declaration of Publication for Bachelor's and Master's Thesis

Studierenden-Angaben / Student Information:

Matrikelnr./ Student ID	**6055390**
Nachname / Surname	**Lühning**
Vorname / First Name	**Nina**

Titel der Arbeit / Title of Thesis

Measurement of NO2-profiles using a drone-mounted DOAS-spectrometer

A) Eigenständigkeitserklärung / Declaration of Authorship

Ich versichere, dass ich die vorliegende Arbeit selbstständig verfasst und keine anderen als die angegebenen Quellen und Hilfsmittel verwendet habe. Alle Teile meiner Arbeit, die wortwörtlich oder dem Sinn nach anderen Werken entnommen sind, wurden unter Angabe der Quelle kenntlich gemacht. Gleiches gilt auch für Zeichnungen, Skizzen, bildliche Darstellungen sowie für Quellen aus dem Internet, dazu zählen auch KI-basierte Anwendungen oder Werkzeuge.
Die Arbeit wurde in gleicher oder hnlicher Form noch nicht als Prüfungsleistung eingereicht.

I hereby affirm that I have written the present work independently and have used no sources or aids other than those indicated. All parts of my work that have been taken from other works, either verbatim or in terms of meaning, have been marked as such, indicating the source. The same applies to drawings, sketches, pictorial representations and sources from the Internet, including AI-based applications or tools. The work has not yet been submitted in the same or a similar form as a final examination paper.

☐ Ich habe KI-basierte Anwendungen und/oder Werkzeuge genutzt und diese im Anhang "Nutzung KI basierte Anwendungen" dokumentiert.

I have used AI-based applications and/or tools and documented them in the appendix "Use of AI-based applications".

B) **Erklärung zur Veröffentlichung von Bachelor- oder Masterarbeiten**
Declaration regarding the publication of bachelor's or master's thesis

Die Abschlussarbeit wird zwei Jahre nach Studienabschluss dem Archiv der Universität Bremen zur dauerhaften Archivierung angeboten. Archiviert werden:

Two years after graduation, the thesis is offered to the archive of the University of Bremen for permanent archiving. The following are archived:

1) Masterarbeiten mit lokalem oder regionalem Bezug sowie pro Studienfach und Studienjahr 10 % aller Masterarbeiten
Master's theses with a local or regional focus, as well as per subject and academic year 10 % of all Master's thesis

2) Bachelorarbeiten des jeweils ersten und letzten Bachelorabschlusses pro Studienfach und Jahr.
Bachelor's thesis for the first and last bachelor's degrees per subject and year.

☑ Ich bin damit einverstanden, dass meine Abschlussarbeit im Universitätsarchiv für wissenschaftliche Zwecke von Dritten eingesehen werden darf.
I agree that my thesis may be viewed by third parties in the university archive for academic purposes.

☑ Ich bin damit einverstanden, dass meine Abschlussarbeit nach 30 Jahren (gem. §7 Abs. 2 BremArchivG) im Universitätsarchiv für wissenschaftliche Zwecke von Dritten eingesehen werden darf.
I agree that my thesis may be viewed by third parties for academic purposes in the university archive after 30 years in accordance with para. 2 BremArchivG).

☐ Ich bin **nicht** damit einverstanden, dass meine Abschlussarbeit im Universitätsarchiv für wissenschaftliche Zwecke von Dritten eingesehen werden darf.
I do not consent to my thesis being made available in the university archive for third parties to view for academic purposes.

C) Einverständniserklärung zur elektronischen Überprüfung der Arbeit auf Plagiate
Declaration of consent for electronic checking of the work for plagiarism

Eingereichte Arbeiten können nach § 18 des Allgemeinen Teil der Bachelor- bzw. der Masterprüfungsordnungen der Universität Bremen mit qualifizierter Software auf Plagiatsvorwürfe untersucht werden.
Zum Zweck der Überprüfung auf Plagiate erfolgt das Hochladen auf den Server der von der Universität Bremen aktuell genutzten Plagiatssoftware.

Submitted papers can be checked for plagiarism using qualified software in accordance with § 18 of the General Section of the Bachelor's or Master's Degree Examination Regulations of the University of Bremen. For the purpose of checking for plagiarism, the upload to the server is done using the plagiarism software currently used by the University of Bremen.

☑ Ich bin damit einverstanden, dass die von mir vorgelegte und verfasste Arbeit zum oben genannten Zweck dauerhaft auf dem externen Server der aktuell von der Universität Bremen genutzten Plagiatssoftware, in einer institutionseigenen Bibliothek (Zugriff nur durch die Universität Bremen), gespeichert wird.

I agree that the work I have submitted and written will be stored permanently on the external server of the plagiarism software currently used by the University of Bremen, in a library belonging to the institution accessed only by the University of Bremen), for the above-mentioned purpose.

☐ Ich bin **nicht** damit einverstanden, dass die von mir vorgelegte und verfasste Arbeit zum o.g. Zweck dauerhaft auf dem externen Server der aktuell von der Universität Bremen genutzten Plagiatssoftware, in einer institutionseigenen Bibliothek (Zugriff nur durch die Universität Bremen), gespeichert wird.

I do not consent to the work I submitted and wrote being permanently stored on the external server of the plagiarism software currently used by the University of Bremen, in a library belonging to the institution accessed only by the University of Bremen), for the above-mentioned purpose.

Das Einverständnis der dauerhaften Speicherung des Textes ist freiwillig. Die Einwilligung kann jederzeit durch Erklärung gegenüber der Universität Bremen, mit Wirkung für die Zukunft, widerrufen werden. Weitere Informationen zur Überprüfung von schriftlichen Arbeiten durch die Plagiatsoftware sind im Nutzungs- und Datenschutzkonzept enthalten. Diese finden Sie auf der Internetseite der Universität Bremen.

Consent to the permanent storage of the text is voluntary. Consent can be withdrawn at any time by making a declaration to this effect to the University of Bremen, with effect for the future. Further information on the checking of written work using plagiarism software can be found in the data protection and usage concept. This can be found on the University of Bremen website.

Mit meiner Unterschrift versichere ich, dass ich die obenstehenden Erklärungen gelesen und verstanden habe und bestätige die Richtigkeit der gemachten Angaben.

With my signature, I confirm that I have read and understood the above explanations and confirm the accuracy of the information provided.

15.09.2026

Datum / Date



Unterschrift als Scan/ Signature